

Automatic design of fiber-reinforced soft actuators for trajectory matching

Fionnuala Connolly^a, Conor J. Walsh^{a,b,1}, and Katia Bertoldi^{a,c,1}

^aHarvard John A. Paulson School of Engineering and Applied Sciences, Cambridge, MA 02138; ^bWyss Institute for Biologically Inspired Engineering, Harvard University, Cambridge, MA 02138; and ^cKavli Institute, Harvard University, Cambridge, MA 02138

Edited by David A. Weitz, Harvard University, Cambridge, MA, and approved November 21, 2016 (received for review September 12, 2016)

Soft actuators are the components responsible for producing motion in soft robots. Although soft actuators have allowed for a variety of innovative applications, there is a need for design tools that can help to efficiently and systematically design actuators for particular functions. Mathematical modeling of soft actuators is an area that is still in its infancy but has the potential to provide quantitative insights into the response of the actuators. These insights can be used to guide actuator design, thus accelerating the design process. Here, we study fluid-powered fiber-reinforced actuators, because these have previously been shown to be capable of producing a wide range of motions. We present a design strategy that takes a kinematic trajectory as its input and uses analytical modeling based on nonlinear elasticity and optimization to identify the optimal design parameters for an actuator that will follow this trajectory upon pressurization. We experimentally verify our modeling approach, and finally we demonstrate how the strategy works, by designing actuators that replicate the motion of the index finger and thumb.

soft robotics | fiber-reinforced actuators | customized actuators

In the field of robotics, it is essential to understand how to design a robot such that it can perform a particular motion for a target application. For example, this robot could be a robot arm that moves along a certain path or a wearable robot that assists with motion of a limb. For conventional hard robots, methods have been developed to describe the forward kinematics (i.e., for given actuator inputs, what will the configuration of the robot be) and inverse kinematics (i.e., for a desired configuration of the robot, what should the actuator inputs be) (1–4).

Recently, there has been significant progress in the field of soft robotics, with the development of many soft grippers (5, 6), locomotion robots (7, 8), and assistive devices (9). Although their inherent compliance, easy fabrication, and ability to achieve complex output motions from simple inputs have made soft robots very popular (10, 11), there is growing recognition that the development of methods for efficiently designing actuators for particular functions is essential to the advancement of the field. To this end, some research groups have begun focusing their efforts on modeling and characterizing soft actuators (12–20). In particular, significant progress has been made on solving the forward kinematics problem (16–19) and even on using dynamic modeling to perform motion planning (14). However, the practical problem of designing a soft actuator to achieve a particular motion remains an issue. Finite element (FE) analysis has previously been used as a design tool to find the optimal geometric parameters for a soft pneumatic actuator, given some design criteria (15). Although this procedure yields some nice results, only basic motions (linear or bending) were studied, because the method is computationally intensive. An alternative approach is to use analytical modeling combined with optimization to determine the properties of a soft actuator that will achieve a particular motion for some target application.

Here, we focus on fiber-reinforced actuators (17–21), and given a particular trajectory, we find the optimal design param-

eters for an actuator that will replicate that trajectory upon pressurization. To achieve this goal, we first use a nonlinear elasticity approach to derive analytical models that provide a relationship between the actuator design parameters (geometry and material properties) and the actuator deformation as a function of pressure for each motion type of interest (extending, expanding, twisting, and bending). Then, we use optimization to determine properties for actuators that match the desired trajectory (Fig. 1). Whereas similar actuators were previously designed empirically (22, 23), here, we propose a robust and efficient strategy to streamline the design process. Furthermore, this strategy is not limited to the specific cases presented here (namely the trajectories of the index finger and thumb) but, rather, could be applied to produce required trajectories in a variety of soft robotic systems, such as locomotion robots, assembly line robots, or devices for pipe inspection.

Analytical Modeling of Actuator Segments

Our approach is based on assuming a desired actuator consists of multiple segments (mimicking the links and joints of the biological digit), where each different segment undergoes some combination of axial extension, radial expansion, twisting about its axis, and bending upon pressurization. To realize actuators capable of replicating complex motions, we use segments consisting of a cylindrical elastomeric tube surrounded by fibers arranged in a helical pattern at a characteristic fiber angle α (Fig. 24) (23, 24), because it has been shown that by varying the fiber angle and materials used, these segments can be easily tuned to achieve a wide range of motions (17–21). When the elastomeric tube is of uniform stiffness, the segment undergoes some combination of

Significance

Fluid-powered elastomeric soft robots have been shown to be able to generate complex output motion using a simple control input such as pressurization of a working fluid. This capability, which mimics similar functions often found in biology, results from variations in mechanical properties of the soft robotic body that cause it to strain to different degrees when stress is applied with the fluid. In this work, we outline a mechanics- and optimization-based approach that enables the automatic selection of mechanical properties of a fiber-reinforced soft actuator to match the kinematic trajectory of the fingers or thumb during a grasping operation. This methodology can be readily extended to other applications that require mimicking or assisting biological motions.

Author contributions: F.C., C.J.W., and K.B. designed research; F.C. performed research; F.C. and K.B. analyzed data; and F.C., C.J.W., and K.B. wrote the paper.

The authors declare no conflict of interest.

This article is a PNAS Direct Submission.

¹To whom correspondence may be addressed. Email: walsh@seas.harvard.edu or bertoldi@seas.harvard.edu.

This article contains supporting information online at www.pnas.org/lookup/suppl/doi:10.1073/pnas.1615140114/-DCSupplemental.

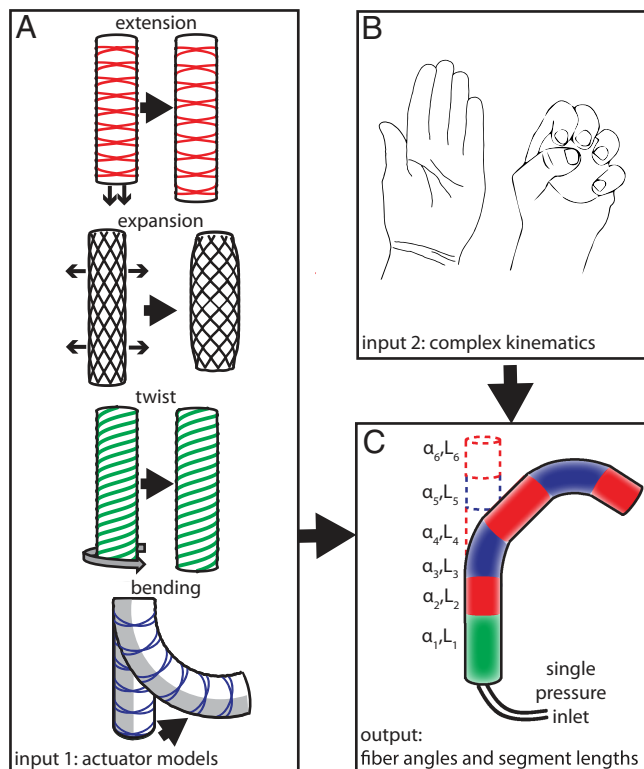


Fig. 1. Designing an actuator that replicates a complex input motion. (A) Analytical models of actuator segments that can extend, expand, twist, or bend are the first input to the design tool. (B) The second input to the design tool is the kinematics of the desired motion. (C) The design tool outputs the optimal segment lengths and fiber angles for replicating the input motion.

axial extension, radial expansion, and twisting about its axis upon pressurization (17–19). In contrast, when the tube is composed of two elastomers of different stiffness, pressurization produces a bending motion (25, 26).

Previous work has explored the design space of fiber-reinforced actuators capable of extending, expanding, and twisting using FE analysis (20) and kinematics and kinestatics modeling (17–19). Although these existing analytical models provide great insight into the behavior of fiber-reinforced actuators, they are restricted to exactly two sets of fibers (a set of fibers being fibers arranged at the same angle).

Here, we use a nonlinear elasticity approach, which facilitates modeling actuators with an arbitrary number of sets of fibers. Rather than modeling the tube and the fibers individually, we treat them as a homogeneous anisotropic material (27–29). More specifically, because the fibers are located on the outside of the tube and not dispersed throughout its thickness, we model the actuator as a hollow cylinder of isotropic incompressible hyperelastic material (corresponding to the elastomer), surrounded by a thin layer of anisotropic material (corresponding to the fiber reinforcement), and impose continuity of deformation between the two layers (Fig. 2A). The isotropic core has initial inner radius R_i and outer radius R_m , and the outer anisotropic layer has initial outer radius R_o . The anisotropic material has a preferred direction that is determined by the initial fiber orientation $\mathbf{S} = (0, \cos \alpha, \sin \alpha)$. We define a deformation gradient \mathbf{F} , from which we calculate the left Cauchy–Green deformation tensor $\mathbf{B} = \mathbf{F}\mathbf{F}^T$, the current fiber orientation $\mathbf{s} = \mathbf{F}\mathbf{S}$, and the tensor invariants $I_1 = \text{tr}(\mathbf{B})$ and $I_4 = \mathbf{s} \cdot \mathbf{s}$.

The inner and outer layers require different strain energy expressions, so let $W^{(in)}$ be the strain energy for the isotropic core and $W^{(out)}$ be the strain energy for the anisotropic outer layer. For the isotropic core, we choose a simple incompressible neo-Hookean model, so that $W^{(in)} = \mu/2(I_1 - 3)$, with μ denoting the initial shear modulus. For the anisotropic layer, let $W^{(out)}$ be the sum of two components, $W^{(out)} = c_1 W^{(iso)} + c_2 W^{(aniso)}$, where $W^{(iso)} = \mu/2(I_1 - 3)$ is the contribution from the isotropic elastomeric matrix, $W^{(aniso)}$ is the contribution from the fibers, and c_1 and c_2 are the corresponding volume fractions. To derive a suitable expression for $W^{(aniso)}$, we consider a small section of the helical fiber and model it as a rod subject to an axial load (SI Appendix, Fig. S5). It is trivial to show that the strain energy density of the rod is (SI Appendix)

$$W^{(aniso)} = \frac{E(\sqrt{I_4} - 1)^2}{2}, \quad [1]$$

where E is its Young's modulus. By slightly modifying the strain energy, the above equations can easily be extended to account for more than one set of fibers. For example, to achieve a pure extending actuator, we might require two sets of fibers, with fiber orientations \mathbf{s}_1 and \mathbf{s}_2 . In this case, the strain energy density is

$$W^{(aniso)} = \frac{E(\sqrt{I_4} - 1)^2}{2} + \frac{E(\sqrt{I_6} - 1)^2}{2}, \quad [2]$$

where $I_4 = \mathbf{s}_1 \cdot \mathbf{s}_1$ and $I_6 = \mathbf{s}_2 \cdot \mathbf{s}_2$.

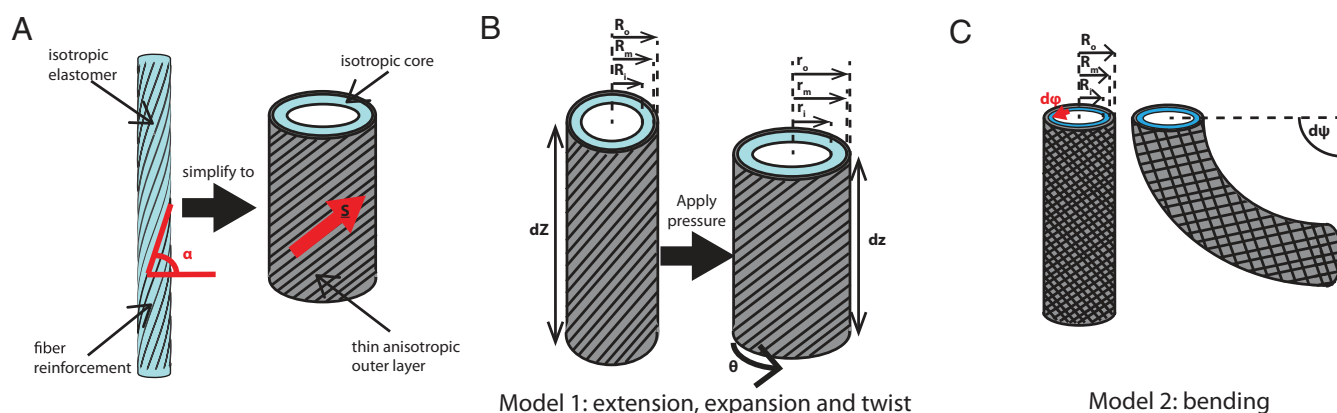


Fig. 2. Modeling a fiber-reinforced actuator. (A) The actuator consists of an elastomeric tube surrounded by an arrangement of fibers. In the model, this system is simplified to an isotropic tube, with an outer layer of anisotropic (but homogeneous) material. (B) Parameters for the analytical model of an extending, expanding, twisting actuator. (C) Parameters for the analytical model of a bending actuator.

Because the actuator bends due to the moment created by the internal pressure acting on the actuator caps (*SI Appendix, Fig. S9*), we equate this moment

$$M_{cap} = 2PR_i^2 \int_0^\pi \sin^2 \phi \text{abs}(R_i \cos \bar{\phi} - R_i \cos \phi) d\phi, \quad [10]$$

with the opposing moment due to the stress in the material

$$M_{mat} = \int \int \lambda_z^{-1} \sigma_{zz}(R_i + \tau) (R_i \cos \bar{\phi} - (R_i + \tau) \cos \phi) d\phi d\tau, \quad [11]$$

where $\bar{\phi}$ denotes the location of the neutral bending axis, $d\tau$ is the differential wall thickness element, and $d\phi$ is the circumferential angle element (Fig. 2C).

Now solving $M_{mat} = M_{cap}$ yields the relationship between input pressure and output bend angle:

$$P = \frac{\int \int \lambda_z^{-1} \sigma_{zz}(R_i + \tau) (R_o \cos \bar{\phi} - (R_i + \tau) \cos \phi) d\phi d\tau}{2R_i^2 \int_0^\pi \sin^2 \phi \text{abs}(R_i \cos \bar{\phi} - R_i \cos \phi) d\phi}, \quad [12]$$

where σ_{zz} can be obtained by substituting **F** into Eqs. 3 and 4 (*SI Appendix*).

Comparing Analytical and Experimental Results. To fabricate the extending, expanding, twisting actuators, we used the elastomer Smooth-Sil 950 ($\mu_2 = 680$ kPa; Smooth-On), and for the bending actuators, we used both Smooth-Sil 950 and Dragon Skin 10 ($\mu_2 = 85$ kPa; Smooth-On). The fiber reinforcement was Kevlar, with a Young's modulus $E = 31,067$ MPa and radius $r = 0.0889$ mm. Each actuator had an inner radius of 6.35 mm, wall thickness of 2 mm, and length of 160 mm. The effective thickness of the fiber layer (8.89×10^{-4} mm) is a fitting parameter here and was identified using the results in *SI Appendix, Fig. S7*.

For the bending model, we used an FE simulation (*SI Appendix, Fig. S10*) to determine the location of the neutral axis ($\phi = 35^\circ$). Using FE analysis, we determined that our bending model was accurate for thin-walled actuators (*SI Appendix, Fig. S11*). However, for thicker-walled actuators, the model yielded lower than expected bend angles at any given pressure. To solve this problem, we used one FE simulation (with fiber angle $\alpha = \pm 5^\circ$) to determine an effective shear modulus $\bar{\mu}$ (78 kPa) for the actuator (rather than using the shear moduli μ_1 and μ_2). We found that using this fitting parameter, we could accurately predict the response for actuators with other fiber angles (*SI Appendix*). Note that because FE analysis generally provides more accurate results than our analytical bending model, an alternative solution would be to use FE simulations to build a database of simulation results for actuators with a range of different fiber angles. However, this option would be more computationally expensive, and so, although not ideal, it is preferable in our case to use just one FE simulation to identify the fitting parameters for the analytical bending model, rather than relying solely on FE.

We first consider extending actuators (with two sets of fibers, arranged symmetrically). Fig. 3A shows how the amount of extension undergone (illustrated by the color) depends on the fiber angle of the actuator (y axis) and the current actuation pressure (x axis). We see that an actuator with fiber angle $\alpha = 0^\circ$ yields the most extension, whereas, in contrast, actuators with larger fiber angles undergo contraction. We fabricated and tested an actuator with fiber angles $\alpha = \pm 3^\circ$ (highlighted in red in Fig. 3A), and the results (Fig. 3B and C) show good agreement between the model and the experiment. Second, we consider twisting actuators, which have only one set of fibers. From Fig. 3D, we can see that an actuator with fiber angle around 30° produces the maximum amount of twist per unit length. Fig. 3E and F shows

that the analytical model accurately represents the twist per unit length undergone by an actuator with fiber angle $\alpha = 3^\circ$.

Finally, Fig. 3G illustrates the bend angle per unit length as a function of fiber angle and actuation pressure. At any given pressure, for larger fiber angles, we see less bend per unit length. Comparing analytical and experimental results for a bending actuator with fiber angles $\alpha = \pm 5^\circ$ (Fig. 3H and I), we see a good match between the model and the experiment.

Replicating Complex Motions

We have presented two analytical models, which describe extending, expanding, twisting, and bending actuator motions. In addition to using these models to explore the actuator design space, we can use them for more complex operations, such as designing a single-input, multisegment actuator that follows a specific trajectory. In the following sections, we will demonstrate this methodology by determining the properties of multisegment actuators that can replicate finger and thumb motion.

The target motion of the actuator was determined using electromagnetic trackers that were placed on the hand at the wrist, at each joint along the finger, and at the fingertip (*SI Appendix, Fig. S13*) (22). Time series data of the coordinates of each sensor in 3D space were recorded as the hand was opened and closed. Using these data, the configuration of the fingers and thumb during a grasping motion can be obtained. Adjacent sensors are connected by links, and we use the data to calculate the length of each link and the angles between the links at each time. We smooth the data by applying a Savitzky–Golay filter. Since it will not be possible to produce an actuator that will match the finger

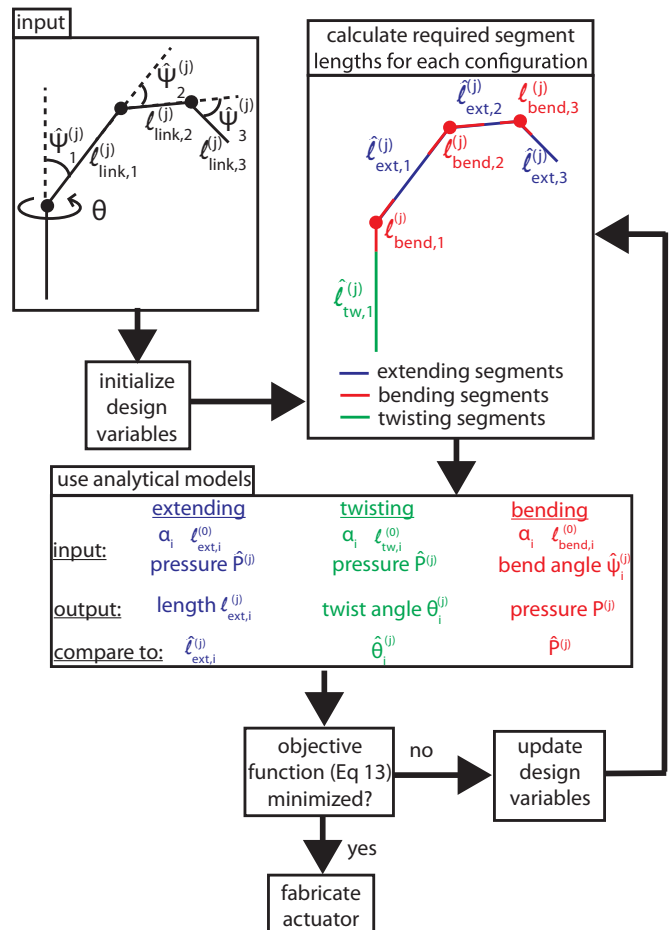


Fig. 4. Optimization algorithm for actuator design.

the current set of variables (P). The parameters $c_1 = 100$ and $c_2 = 1,000$ are weights that balance the relative importance of the twisting, bending, and extending segments. If f is not sufficiently small, the variables are updated and the optimization loop repeats. When the minimum value of f is found, the optimization outputs (i) the fiber angle α_i for each segment, (ii) the initial length of each of the bending and twisting segments, and (iii) the pressures $\hat{P}^{(j)}$ at which the goal configurations will occur.

Index Finger Motion. The fiber angles and lengths required to imitate the movement of the index finger are illustrated in Fig. 5D. Segments 1, 3, and 6 have length 70 mm, 22 mm, and 15 mm, with fiber angles of $\pm 40^\circ$, $\pm 50^\circ$, and $\pm 50^\circ$, respectively. These segments undergo axial contraction when pressurized. Segments 2, 4, and 5 are bending segments of length 22 mm, 28 mm, and 15 mm, with fiber angles of $\pm 6^\circ$, $\pm 5^\circ$ and $\pm 5^\circ$, respectively.

We fabricate the actuator as detailed in *SI Appendix*. To compare the actual performance of the actuator to the expected performance, we characterize it by taking pictures of the actuator at various different actuation pressures. We evaluate its motion by using Matlab to track points on the actuator. We see good agreement between expected and actual motion (Fig. 5C and E and *Movie S1*), with some discrepancies that are most likely due to defects in the actuator fabrication (for example, segment lengths being up to 4 mm shorter than expected, due to the fibers being wound around the actuator between segments; *SI Appendix*).

Thumb Motion. As a second example, we consider the design of an actuator that upon pressurization, replicates the motion of a thumb. The motion of the thumb is more complex than that of the finger, because it moves out of plane. We capture this out-of-plane motion as a twisting motion. We calculate the amount of twist by fitting a plane to the twisting links at each time and then finding the angle between the normal to this plane and the normal to the initial plane.

Fig. 5I illustrates the fiber angles that are needed to reproduce the motion of the thumb, as predicted by the model. Segment 1 is a twisting segment of length 25 mm, with fiber angle 5° ; segments 2, 4, and 6 are bending segments of length 15 mm,

30 mm, and 22 mm, each with fiber angles $\pm 5^\circ$; and segments 3, 5, and 7 are extending segments of length 20 mm, 8 mm, and 17 mm, with fiber angles $\pm 41^\circ$, $\pm 50^\circ$, and $\pm 47^\circ$. To analyze the motion of this actuator, we placed two cameras at right angles to each other and took pictures of the actuator at various different actuation pressures. The images were combined to reproduce the 3D motion of the actuator (*SI Appendix*). Fig. 5H and J compares the input thumb kinematics and the output actuator motion (*Movie S2*). We see reasonable agreement between the expected and achieved motions, with discrepancies in this case most likely due to inaccuracies in measuring the actuator motion (for example, misalignment of cameras), as well as defects in actuator fabrication (such as nonuniform wall thickness).

Conclusions

Using analytical models for fiber-reinforced actuators that extend, expand, twist, and bend, we have devised a method of designing actuators customized for a particular function. Given the kinematics of the required motion, and the number and type of segments required, the algorithm outputs the appropriate length and fiber angle of each segment, thereby providing a recipe for how the actuator should be made. The procedure is somewhat limited in its current form because it requires the user to input the type of segments required, but future versions will eliminate the need for this step, thus further automating the procedure. Future work will also focus on developing a model that combines bending with other motions, to increase the versatility of the algorithm. The design tool we have presented here has immense potential to streamline and accelerate the design of soft actuators for a particular task, eliminating much of the trial and error procedure that is currently used and broadening the scope of fiber-reinforced soft actuators.

ACKNOWLEDGMENTS. The authors thank Dr. J. Weaver for assistance with 3D printing and Dr. P. Polygerinos and Dr. S. Sanan for helpful discussions. This work was partially supported by National Science Foundation Grant 1317744, the Materials Research Science and Engineering Center under National Science Foundation Award DMR-1420570, the Wyss Institute, and Harvard's Paulson School of Engineering and Applied Sciences.

- Denavit J, Hartenberg RS (1955) A kinematic notation for lower pair mechanisms based on matrices. *J Appl Mech* 22:215–221.
- Murray RM, Li Z, Sastry SS (1994) *A Mathematical Introduction to Robotic Manipulation* (CRC Press, Boca Raton, FL).
- Aristidou A, Lasenby J (2009) Inverse Kinematics: A Review of Existing Techniques and Introduction of a New Fast Iterative Solver (University of Cambridge, Cambridge, UK).
- Colome A, Torras C (2012) Redundant inverse kinematics: Experimental comparative review and two enhancements (IEEE/RSJ Int Conf Intell Robot Syst, Vilamoura, Portugal), pp 5333–5340.
- Suzumori K, Iikura S, Tanaka H (1992) Applying a flexible microactuator to robotic mechanisms. *IEEE Control Syst* 12(1):21–27.
- Martinez RV, et al. (2013) Robotic tentacles with three-dimensional mobility based on flexible elastomers. *Adv Mater* 25(2):205–212.
- Marchese AD, Onal CD, Rus D (2014) Autonomous soft robotic fish capable of escape maneuvers using fluidic elastomer actuators. *Soft Robot* 1(1):75–87.
- Tolley MT, et al. (2014) A resilient, untethered soft robot. *Soft Robot* 1(3):213–223.
- Connolly L, et al. (2009) Use of a pneumatic glove for hand rehabilitation following stroke. *Conf Proc IEEE Eng Med Biol Soc* 2009:2434–2437.
- Rus D, Tolley MT (2015) Design, fabrication and control of soft robots. *Nature* 521(7553):467–475.
- Majidi C (2013) Soft robotics: a perspective - current trends and prospects for the future. *Soft Robot* 1(1):5–11.
- Hirai S, et al. (2000) Qualitative synthesis of deformable cylindrical actuators through constraint topology. *IEEE/RSJ Int Conf Intell Robot Syst* 1:197–202.
- Case JC, White EL, Kramer RK (2015) Soft material characterization for robotic applications. *Soft Robot* 2(2):80–87.
- Marchese AD, Tedrake R, Rus D (2016) Dynamics and trajectory optimization for a soft spatial fluidic elastomer manipulator. *Int J Rob Res* 35(8):1000–1019.
- Moseley P, et al. (2016) Modeling, design, and development of soft pneumatic actuators with finite element method. *Adv Eng Mater* 18(6):978–988.
- Polygerinos P, et al. (2015) Modeling of soft fiber-reinforced bending actuators. *IEEE Trans Robot* 31(3):778–789.
- Singh G, Krishnan G (2015) An isoperimetric formulation to predict deformation behavior of pneumatic fiber reinforced elastomeric actuators (IEEE/RSJ Int Conf Intell Robot Syst, Hamburg, Germany), pp 1738–1743.
- Krishnan G, Bishop-Moser J, Kim C, Kota S (2015) Kinematics of a generalized class of pneumatic artificial muscles. *J Mech Robot* 7(4):041014.
- Bishop-Moser J, Kota S (2015) Design and modeling of generalized fiber-reinforced pneumatic soft actuators. *IEEE Trans Robot* 31(3):536–545.
- Connolly F, Polygerinos P, Walsh CJ, Bertoldi K (2015) Mechanical programming of soft actuators by varying fiber angle. *Soft Robot* 2(1):26–32.
- Galloway KC, Polygerinos P, Walsh CJ, Wood RJ (2013) Mechanically programmable bend radius for fiber-reinforced soft actuators (Int Conf Adv Robot, Montevideo, Uruguay), pp 1–6.
- Polygerinos P, Wang Z, Galloway KC, Wood RJ, Walsh CJ (2015) Soft robotic glove for combined assistance and at-home rehabilitation. *Rob Auton Syst* 73:135–143.
- Galloway K, et al. (2015) Multi-segment reinforced actuators and applications. US Patent WO 2015066143 A1.
- Bishop-Moser J, Krishnan G, Kota S (2015) Fiber-reinforced actuator. US Patent US 20150040753 A1.
- Suzumori K, Iikura S, Tanaka H (1991) Flexible microactuator for miniature robots (Proc IEEE Micro Electro Mech Syst, Nara, Japan), pp 204–209.
- Firouzeh A, Salerno M, Paik J (2015) Soft pneumatic actuator with adjustable stiffness layers for multi-DoF actuation (IEEE/RSJ Int Conf Intell Robot Syst, Hamburg, Germany), pp 1117–1124.
- Adkins JE, Rivlin RS (1955) Large elastic deformations of isotropic materials X. Reinforcement by inextensible cords. *Philos Trans R Soc Lond A* 248(944):201–223.
- Kassianidis F (2007) Boundary-value problems for transversely isotropic hyperelastic solids. PhD Thesis (University of Glasgow, Glasgow, UK).
- Goriely A, Tabor M (2013) Rotation, inversion, and perversion in anisotropic elastic cylindrical tubes and membranes. *Proc Math Phys Eng Sci* 469(2153):20130011.
- Holzappel GA (2000) *Nonlinear Solid Mechanics. A Continuum Approach for Engineering* (Wiley, Chichester, NY).
- Ogden RW (1984) *Non-Linear Elastic Deformations* (Dover, New York).

SI Appendix for

Automatic design of fiber-reinforced soft actuators for trajectory matching

Fionnuala Connolly*, Conor J. Walsh*,[†], Katia Bertoldi*,[‡]

*Harvard John A. Paulson School of Engineering and Applied Sciences, Cambridge, MA 02138

[†]Wyss Institute, Harvard University, Cambridge, MA 02138

[‡]Kavli Institute Harvard University, Cambridge, MA 02138

S1 Actuator fabrication and material characterization

In this section, we describe our methods for fabricating fiber-reinforced soft actuators. We first describe how to fabricate actuators which extend, expand, and twist, then actuators which bend, and finally, segmented actuators. We describe our procedure for molding the elastomeric tube, and for winding the fibers at a particular angle. We also describe the procedure for characterizing the elastomers used.

S1.1 Extending/Expanding/Twisting actuators

The actuator mold is designed in Solidworks and 3d printed using an Objet Connex 500 printer (Stratasys) (see Figure S1A). The mold is assembled and held together firmly with clamps. Elastomer is poured into the mold (Figure S1B), and degassed in a vacuum chamber for a couple of minutes. A cylindrical metal rod is inserted into the mold to create the core of the actuator. The rod slots into a round indentation at the bottom of the mold and a 3d printed cap holds the rod in place at the top of the mold (Figure S1C). The elastomer is left overnight at room temperature to cure.

The next day, the plastic mold is removed. Kevlar fiber is wound in a helical pattern around the outside of the actuator (Figure S1D). Ridges on the surface of the mold leave grooves on the actuator, which define the path for winding the fibers. In this way, we have precise control over the fiber angle. At each end of the actuator, the fiber is looped around a few times and tied. These knots are held in place by applying a small amount of Sil-Poxy (Smooth-On, Inc.). The actuator is then removed from the rod using isopropanol as a lubricant. The ends of the actuator are plugged with Sil-Poxy, and a vented screw is inserted at one end. The Sil-Poxy is allowed to cure for 24 hours.

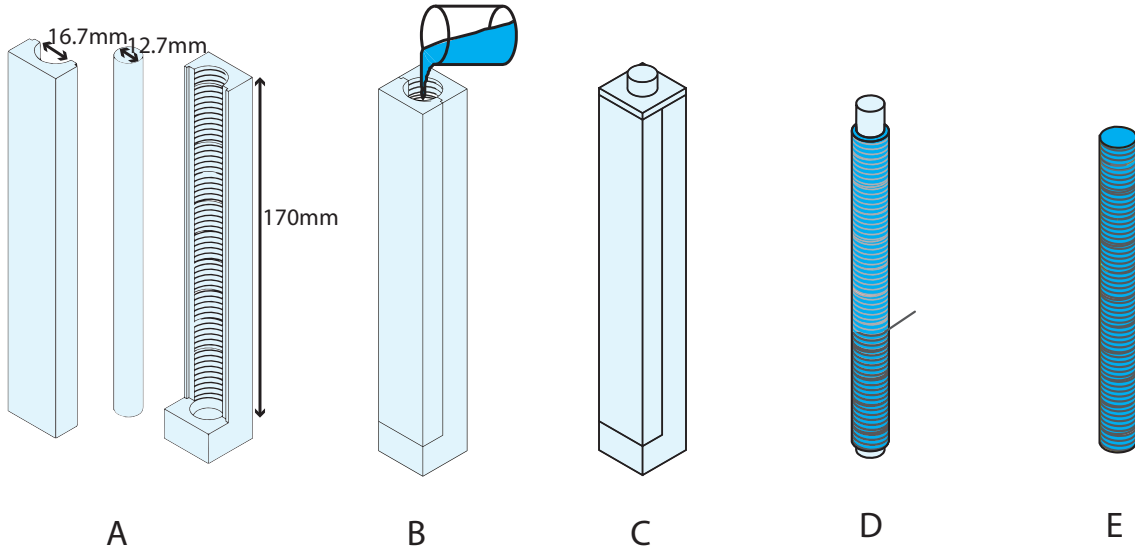


Figure S1: Fabrication of an extending/expanding/twisting actuator. (A) A metal rod and 3d printed mold are used to mold the elastomer. (B) Elastomer is poured into the mold. (C) The rod is inserted into the mold and held in place with a 3d printed cap. (D) The mold is removed and Kevlar fiber is wound around the outside of the actuator. (E) The actuator is capped with Sil-Poxy.

S1.2 Bending actuators

The fabrication procedure for bending actuators is similar to the procedure for extending/expanding/twisting actuators. The only difference is that the cylindrical tube is composed of two different elastomers. To fabricate the first half of this tube, one side of the 3d printed mold is laid down flat, and Elastomer 1 is poured into the mold (Figure S2A). The metal rod is placed on top of the elastomer, and slots into place at the top and bottom of the mold. This is left to cure overnight in a pressure chamber (curing at high pressure reduces the size of any air bubbles present in the elastomer). The next day, the edges of the elastomer are trimmed (without removing it from the mold) so that it forms a perfect half-cylinder. Elastomer 2 (of different stiffness to Elastomer 1) is poured on top of the metal rod (Figure S2B), and the top half of the mold is quickly placed on top. The two halves of the mold are held together firmly with clamps. Again, this is left overnight in a pressure chamber to allow the second elastomer to cure (Figure S2C). The remainder of the procedure is the same as for the extending/expanding/twisting actuators.

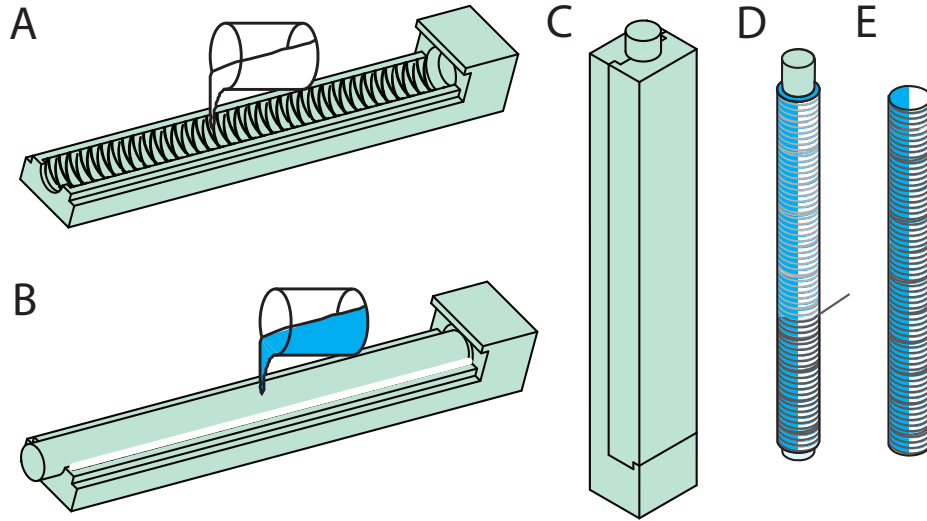


Figure S2: Fabrication of a bending actuator (A) The first half of the mold is laid down flat and Elastomer 1 is poured in. (B) When Elastomer 1 has cured, Elastomer 2 is poured on top. (C) The second half of the mold is placed on top and Elastomer 2 is left to cure. (D) The mold is removed and Kevlar fiber is wound around the outside of the actuator. (E) The actuator is capped with Sil-Poxy.

S1.3 Segmented actuators

A segmented actuator consists of some bending actuator segments and some extending/twisting actuator segments. One half of the actuator is made entirely of Elastomer 1. The other half is made of Elastomer 1 if it is a twisting and/or extending segment, and Elastomer 2 (different stiffness) if it is a bending segment. Therefore, a segmented mold is used, as shown in Figure S3A.

First, the whole mold is assembled and held together with clamps, and the actuator is cast entirely from Elastomer 1 (Figure S3B,C). Then one side of the mold (the segmented side) is removed. The segments are then fabricated one by one. As shown in Figure S3D,E, the exposed elastomer is cut away, and the new elastomer is poured (Elastomer 1 or 2, depending on the type of segment). The elastomer is cut away segment by segment like this so that every time new elastomer is being poured, it is being poured on a freshly exposed surface. This improves the bond between the elastomers. To speed up the process, the elastomer is cured in the oven for 30 minutes at 60°C (rather than overnight at room temperature). When all of the segments have cured, the mold is removed, and fibers are wrapped around the outside of the actuator.

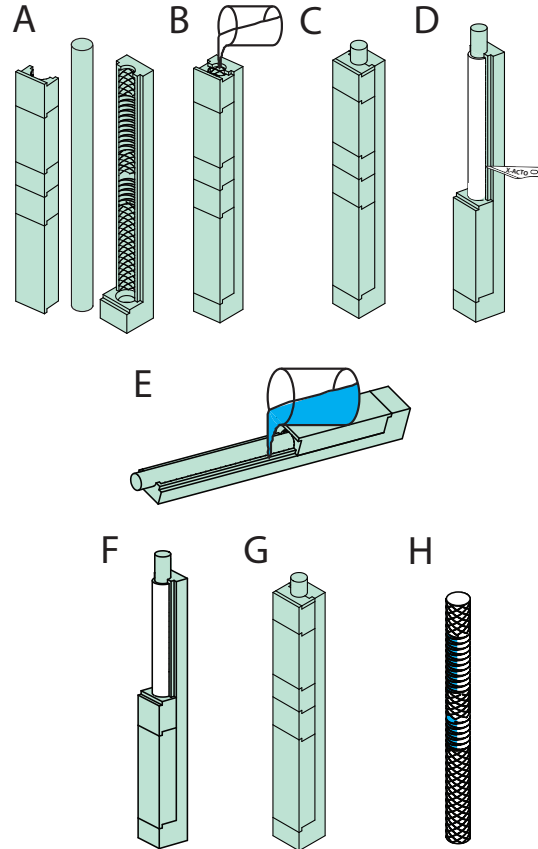


Figure S3: Fabrication of a segmented actuator. (A) A metal rod and 3d printed mold are used to mold the elastomer. (B) First, Elastomer 1 is used to make the entire actuator. (C) Elastomer 1 is left to cure. (D)-(G) The elastomeric segments are fabricated one by one. (H) The mold is removed and the actuator is capped with Sil-Poxy.

S1.3.1 Actuator segment lengths

In tables 1-4 we report the intended initial lengths of each of the segments in the finger and thumb actuators (as prescribed by the optimization algorithm - see Section S4) and compare them to the actual segment lengths in the actuators we fabricated. The discrepancies are due to small inconsistencies in the fabrication procedure, as well as the space taken up by the fibers wound around the actuator between segments.

Index Finger Segments						
segment	1	2	3	4	5	6
required initial length (<i>mm</i>)	70	22	22	28	15	15
actual initial length (<i>mm</i>)	66	20	18	28	15	12
% error	6	9	18	0	0	20

Table 1: Comparison of required segment length with achieved segment length for each segment of the finger actuator

Index Finger Links				
link	1	2	3	4
required initial length (<i>mm</i>)	81	47	21.5	22.5
actual initial length (<i>mm</i>)	76	42	21.5	19.5
% error	6	11	0	13

Table 2: Comparison of required link length with achieved link length for each link of the finger actuator

Thumb Segments							
segment	1	2	3	4	5	6	7
required initial length (<i>mm</i>)	25	15	20	30	8	22	17
actual initial length (<i>mm</i>)	25	16	18	27	7	22	17
% error	0	7	10	10	13	0	0

Table 3: Comparison of required segment length with achieved segment length for each segment of the thumb actuator

Thumb Links			
link	1	2	3
required initial length (<i>mm</i>)	42.5	34	28
actual initial length (<i>mm</i>)	39.5	31.5	28
% error	7	7	0

Table 4: Comparison of required link length with achieved link length for each link of the thumb actuator

S1.4 Material Characterization

Dogbone-shaped samples (ASTM standard) made out of the elastomers used to fabricate the actuators (Smooth-Sil 950 and Dragon Skin 10, Smooth-on Inc., PA, USA) were tested under uniaxial tension using a single-axis Instron (model 5566; Instron, Inc.) with a 100N load cell. The material behavior up to a stretch of 2.5 is reported in Figure S4. We used a least squares method to fit an incompressible Neo-Hookean model to the measured data, and found that the material response is best captured with an initial shear modulus $\mu = 0.085$ MPa for Dragon Skin 10 and $\mu = 0.68$ MPa for Smooth-Sil 950.

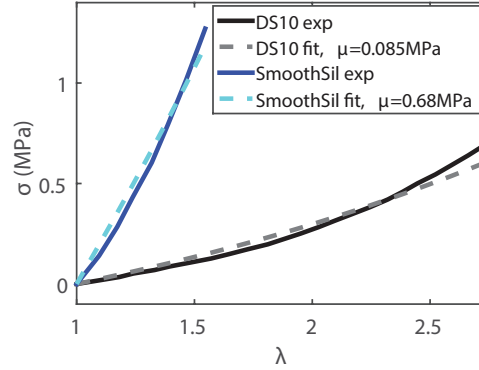


Figure S4: Experimental stress-strain data and a best-fit neo-Hookean model for Dragonskin 10 and SmoothSil 950 under uniaxial tensile loading

S2 Finite Element Simulations

As well as performing experiments, we performed finite element simulations as additional verification for our analytical modeling. All finite element simulations were carried out using the commercial finite element software Abaqus (SIMULIA, Providence, RI). In each case, the elastomer was modeled as an incompressible neo-Hookean material. The Kevlar fibers were modeled as a linearly elastic material using the manufacturer's specifications: diameter 0.1778mm , Young's modulus $31.067 \times 10^6 \text{kPa}$ and Poisson's ratio 0.36. For the elastomer, 20-node quadratic brick elements, with reduced integration (Abaqus element type C3D20R) were used, and 3-node quadratic beam elements (Abaqus element type B32) were used for the fibers. Perfect bonding between the fibers and the elastomer was assumed (the fibers were connected to the elastomer by tie constraints). Quasi-static non-linear simulations were performed using Abaqus/Standard. One end of the actuator was held fixed, and a pressure load was applied to the inner surface of the actuator.

Note that sample files for running Abaqus simulations can be found on softroboticstoolkit.com.

S3 Analytical modeling

In this section, we present analytical models for fiber-reinforced actuators which extend, expand, twist, and bend. We use a non-linear elasticity approach to analytically model the response of the fiber-reinforced actuators free to deform under pressurization. Rather than modeling the tube and the fibers individually, we treat them as a homogeneous anisotropic material [1-3]. More specifically, as the fibers are located on the outside of the tube and not dispersed throughout its thickness, we model the actuator as a hollow cylinder of isotropic incompressible hyperelastic material (corresponding to the elastomer), surrounded by a thin layer of anisotropic material (corresponding to the fiber reinforcement), and impose continuity of deformation between the two layers (Figure 2A of the main text). The isotropic core has initial inner radius R_i and outer radius R_m , while the outer anisotropic layer has initial outer radius R_o . The anisotropic material has a preferred direction which is determined by the initial fiber orientation $\mathbf{S} = (0, \cos \alpha, \sin \alpha)$, where α is the fiber angle.

In the following, we first construct the strain energy expressions for both the inner and outer layers. Then, to simplify the analytical modeling, we decouple bending from the other motions, so we first introduce a model for actuators which extend, expand, and twist upon pressurization, followed by a model for actuators which bend upon pressurization. In each case, we use experimental and finite element results to validate the analytical models.

S3.1 Strain energy for the actuators

The inner and outer layers require different strain energy expressions, so let $W^{(in)}$ be the strain energy for the isotropic core, and $W^{(out)}$ be the strain energy for the anisotropic outer layer. For the isotropic core, we choose a simple incompressible neo-Hookean model, so that

$$W^{(in)} = \frac{\mu}{2}(I_1 - 3), \quad (\text{S1})$$

μ denoting the initial shear modulus and $I_1 = \text{tr}(\mathbf{F}\mathbf{F}^T)$, \mathbf{F} being the deformation gradient. For the anisotropic layer, let $W^{(out)}$ be the sum of two components,

$$W^{(out)} = c_1 W^{(iso)} + c_2 W^{(aniso)}, \quad (\text{S2})$$

where $W^{(iso)} = \mu/2(I_1 - 3)$ is the contribution from the isotropic elastomeric matrix, $W^{(aniso)}$ is the contribution from the fibers, and c_i are the corresponding volume fractions. To derive a suitable expression for $W^{(aniso)}$, we consider a helical fiber with cross-sectional area \hat{a} , initial orientation $\mathbf{S} = (0, \cos \alpha, \sin \alpha)$,

and current orientation $\mathbf{s} = \mathbf{F}\mathbf{S}$ subject to an axial load \bar{F} (Figure S5A). We focus on a small segment of the helical fiber of length dl which undergoes a change in length dx . Assuming there is a linear relationship between the force \bar{F} and extension dx (as shown in Figure S5B), the strain energy for the segment, $dW^{(fiber)}$, is equal to the area underneath the force-displacement curve,

$$dW^{(fiber)} = \frac{1}{2}\bar{F}dx. \quad (\text{S3})$$

For the considered linear elastic fiber \bar{F} can be expressed as

$$\bar{F} = E\epsilon\hat{a} \quad (\text{S4})$$

where $\epsilon = dx/dl$ is the axial strain, and E is the Young's modulus. Substituting Equation (S4) into Equation (S3), we have

$$dW^{(fiber)} = \frac{1}{2}\epsilon E\hat{a}dx = \frac{1}{2}\epsilon^2 E\hat{a}dl, \quad (\text{S5})$$

and integrating yields

$$W^{(fiber)} = \int_0^{L_f} \frac{1}{2}\epsilon^2 E\hat{a}dl = \frac{1}{2}\epsilon^2 E\hat{a}L_f, \quad (\text{S6})$$

which is the energy of the helical fibers. Since $I_4 = \mathbf{s} \cdot \mathbf{s}$ is the stretch of the fiber, we have $\epsilon = \sqrt{I_4} - 1$, and substituting this in Equation (S6) yields

$$W^{(fiber)} = \frac{(\sqrt{I_4} - 1)^2 E\hat{a}L_f}{2} \quad (\text{S7})$$

Dividing by the volume of the fiber yields the strain energy density

$$W^{(aniso)} = \frac{(\sqrt{I_4} - 1)^2 E}{2}. \quad (\text{S8})$$

If an actuator has multiple sets of fibers (i.e. fibers arranged at different fiber angles), the strain energy can easily be modified to account for this. For example, suppose the actuator has two sets of fibers: one set at a fiber angle α_1 (i.e. with initial fiber orientation $\mathbf{S}_1 = (0, \cos \alpha_1, \sin \alpha_1)$, and current fiber orientation $\mathbf{s}_1 = \mathbf{F}\mathbf{S}_1$), and one set at a fiber angle α_2 (i.e. with initial fiber orientation $\mathbf{S}_2 = (0, \cos \alpha_2, \sin \alpha_2)$, and current fiber orientation $\mathbf{s}_2 = \mathbf{F}\mathbf{S}_2$). Then the strain energy is

$$W^{(aniso)} = \frac{(\sqrt{I_4} - 1)^2 E}{2} + \frac{(\sqrt{I_6} - 1)^2 E}{2}, \quad (\text{S9})$$

where $I_4 = \mathbf{s}_1 \cdot \mathbf{s}_1$ and $I_6 = \mathbf{s}_2 \cdot \mathbf{s}_2$. Similarly, for three sets of fibers, we have strain energy

$$W^{(aniso)} = \frac{(\sqrt{I_4} - 1)^2 E}{2} + \frac{(\sqrt{I_6} - 1)^2 E}{2} + \frac{(\sqrt{I_{10}} - 1)^2 E}{2}, \quad (\text{S10})$$

where $I_{10} = \mathbf{s}_3 \cdot \mathbf{s}_3$.

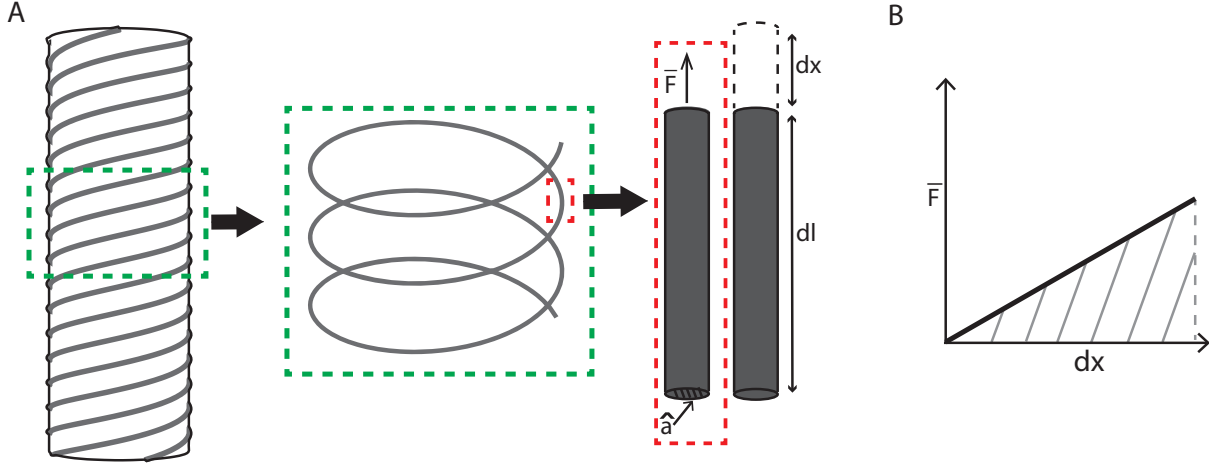


Figure S5: (A) The helical fiber is modeled as a rod, of cross-sectional area \hat{a} , undergoing axial extension dx due to an axial load \bar{F} . (B) We assume the fiber extends linearly with applied force. The strain energy is then equal to the area underneath the force-displacement curve (the shaded area).

S3.2 Modeling extension, expansion, and twist

When the elastomeric part of the actuator is of uniform stiffness, we assume that the tube retains its cylindrical shape upon pressurization, and the radii become r_i , r_m , and r_o in the pressurized configuration (Figure 2B of the main text). The possible extension, expansion, and twisting deformations are then described by

$$\begin{aligned} r^2 - r_o^2 &= \lambda_z^{-1}(R^2 - R_o^2), \\ \theta &= \Theta + \tau \lambda_z Z, \\ z &= \lambda_z Z, \end{aligned} \quad (\text{S11})$$

from which the deformation gradient can be obtained as

$$\mathbf{F} = \begin{pmatrix} \frac{\partial r}{\partial R} & \frac{1}{R} \frac{\partial r}{\partial \Theta} & \frac{\partial r}{\partial Z} \\ r \frac{\partial \theta}{\partial R} & \frac{r}{R} \frac{\partial \theta}{\partial \Theta} & r \frac{\partial \theta}{\partial Z} \\ \frac{\partial z}{\partial R} & \frac{1}{R} \frac{\partial z}{\partial \Theta} & \frac{\partial z}{\partial Z} \end{pmatrix} = \begin{pmatrix} \frac{R}{r \lambda_z} & 0 & 0 \\ 0 & \frac{r}{R} & r \tau \lambda_z \\ 0 & 0 & \lambda_z \end{pmatrix}$$

where R, Φ, Z and r, ϕ, z are the radial, circumferential, and longitudinal coordinates in the reference and current configurations, respectively [2,4]. Moreover, λ_z and τ denote the axial stretch and the twist per unit

length, respectively. The deformation gradient \mathbf{F} is used to calculate the left Cauchy-Green deformation tensor $\mathbf{B} = \mathbf{F}\mathbf{F}^T$ and the current fiber orientation $\mathbf{s} = \mathbf{F}\mathbf{S}$, from which we obtain the tensor invariants $I_1 = \text{tr}(\mathbf{B})$ and $I_4 = \mathbf{s} \cdot \mathbf{s}$. Finally, we can then use the strain energies of Equations S1 and S2 to calculate the Cauchy stresses, which take the form

$$\begin{aligned}\sigma^{(in)} &= 2W_1^{(in)}\mathbf{B} - p\mathbf{I} \\ \sigma^{(out)} &= 2W_1^{(out)}\mathbf{B} + 2W_4^{(out)}\mathbf{s}_1 \otimes \mathbf{s}_1 + 2W_6^{(out)}\mathbf{s}_2 \otimes \mathbf{s}_2 - p\mathbf{I}\end{aligned}\tag{S12}$$

where $W_i = \frac{\partial W}{\partial I_i}$, \mathbf{I} is the identity matrix, and p is a hydrostatic pressure[4].

To determine the current actuator configuration, we first apply the Cauchy equilibrium equations (i.e. $\text{div}(\sigma) = 0$), yielding

$$\frac{d\sigma_{rr}}{dr} = \frac{\sigma_{\theta\theta} - \sigma_{rr}}{r},\tag{S13}$$

which can then be integrated to yield

$$P = \int_{r_i}^{r_m} \frac{\sigma_{\theta\theta}^{(in)} - \sigma_{rr}^{(in)}}{r} dr + \int_{r_m}^{r_o} \frac{\sigma_{\theta\theta}^{(out)} - \sigma_{rr}^{(out)}}{r} dr,\tag{S14}$$

where P is the pressure applied inside the tube. Assuming there are no external axial forces or external axial moments applied to the tube, the axial load N can be obtained as

$$N = 2\pi \int_{r_i}^{r_m} \sigma_{zz}^{(in)} r dr + 2\pi \int_{r_m}^{r_o} \sigma_{zz}^{(out)} r dr = P\pi r_i^2,\tag{S15}$$

while the axial moment M is given by

$$M = 2\pi \int_{r_i}^{r_m} \sigma_{\theta z}^{(in)} r^2 dr + 2\pi \int_{r_m}^{r_o} \sigma_{\theta z}^{(out)} r^2 dr = 0.\tag{S16}$$

Equation (S15) can be manipulated as follows:

$$\begin{aligned}
N &= 2\pi \int_{r_i}^{r_m} \sigma_{zz}^{(in)} r dr + 2\pi \int_{r_m}^{r_o} \sigma_{zz}^{(out)} r dr \\
&= 2\pi \int_{r_i}^{r_m} (\sigma_{zz}^{(in)} - \sigma_{rr}^{(in)} + \sigma_{\theta\theta}^{(in)}) r dr + 2\pi \int_{r_m}^{r_o} (\sigma_{zz}^{(out)} - \sigma_{rr}^{(out)} + \sigma_{\theta\theta}^{(out)}) r dr \\
&= 2\pi \int_{r_i}^{r_m} (\sigma_{zz}^{(in)} - \sigma_{rr}^{(in)}) r dr + 2\pi \left[\frac{\sigma_{rr}^{(in)} r^2}{2} \right]_{r_i}^{r_m} - 2\pi \int_{r_i}^{r_m} \frac{r^2}{2} \frac{d\sigma_{rr}^{(in)}}{dr} \\
&\quad + 2\pi \int_{r_m}^{r_o} (\sigma_{zz}^{(out)} - \sigma_{rr}^{(out)}) r dr + 2\pi \left[\frac{\sigma_{rr}^{(out)} r^2}{2} \right]_{r_m}^{r_o} - 2\pi \int_{r_m}^{r_o} \frac{r^2}{2} \frac{d\sigma_{rr}^{(out)}}{dr} \\
&= 2\pi \int_{r_i}^{r_m} (\sigma_{zz}^{(in)} - \sigma_{rr}^{(in)}) r dr + P\pi r_i^2 - \pi \int_{r_i}^{r_m} r^2 \frac{\sigma_{\theta\theta}^{(in)} - \sigma_{rr}^{(in)}}{r} dr \\
&\quad + 2\pi \int_{r_m}^{r_o} (\sigma_{zz}^{(out)} - \sigma_{rr}^{(out)}) r dr - \pi \int_{r_m}^{r_o} r^2 \frac{\sigma_{\theta\theta}^{(out)} - \sigma_{rr}^{(out)}}{r} dr \\
&= \pi \int_{r_i}^{r_m} (2\sigma_{zz}^{(in)} - \sigma_{rr}^{(in)} - \sigma_{\theta\theta}^{(in)}) r dr + P\pi r_i^2 + \pi \int_{r_m}^{r_o} (2\sigma_{zz}^{(out)} - \sigma_{rr}^{(out)} - \sigma_{\theta\theta}^{(out)}) r dr
\end{aligned} \tag{S17}$$

Combining Equations (S15) and (S17), we have

$$N = \pi \int_{r_i}^{r_m} (2\sigma_{zz}^{(in)} - \sigma_{rr}^{(in)} - \sigma_{\theta\theta}^{(in)}) r dr + P\pi r_i^2 + \pi \int_{r_m}^{r_o} (2\sigma_{zz}^{(out)} - \sigma_{rr}^{(out)} - \sigma_{\theta\theta}^{(out)}) r dr = P\pi r_i^2 \tag{S18}$$

Now canceling the $P\pi r_i^2$ on the left side of the equation with the $P\pi r_i^2$ term on the right side of the equation, we can write the *reduced axial load* (that is, the axial load due to forces other than the applied pressure) [3]

$$N_{ral} = \pi \int_{r_i}^{r_m} (2\sigma_{zz}^{(in)} - \sigma_{rr}^{(in)} - \sigma_{\theta\theta}^{(in)}) r dr + \pi \int_{r_m}^{r_o} (2\sigma_{zz}^{(out)} - \sigma_{rr}^{(out)} - \sigma_{\theta\theta}^{(out)}) r dr = 0. \tag{S19}$$

Finally, defining $\lambda_\theta = \frac{r}{R}$ and $\gamma = r\tau$, and using the identities [2]

$$\begin{aligned}
\sigma_{\theta\theta} - \sigma_{rr} &= \lambda_\theta \frac{\partial W}{\partial \lambda_\theta} + \gamma \frac{\partial W}{\partial \gamma} \\
\sigma_{\theta\theta} + \sigma_{zz} - 2\sigma_{rr} &= \lambda_\theta \frac{\partial W}{\partial \lambda_\theta} + \lambda_z \frac{\partial W}{\partial \lambda_z} \\
\sigma_{\theta z} &= \frac{\partial W}{\partial \gamma},
\end{aligned} \tag{S20}$$

we can write the equilibrium equations in terms of the strain energy:

$$P = \int_{r_i}^{r_m} \lambda_z \frac{\partial W^{(in)}}{\partial \lambda_z} + \gamma \frac{\partial W^{(in)}}{\partial \gamma} \frac{dr}{r} + \int_{r_m}^{r_o} \lambda_z \frac{\partial W^{(out)}}{\partial \lambda_z} + \gamma \frac{\partial W^{(out)}}{\partial \gamma} \frac{dr}{r} \quad (S21)$$

$$N_{ral} = \pi \int_{r_i}^{r_m} 2\lambda_z \frac{\partial W^{(in)}}{\partial \lambda_z} - \lambda_\theta \frac{\partial W^{(in)}}{\partial \lambda_\theta} - 3\gamma \frac{\partial W^{(in)}}{\partial \gamma} r dr + \pi \int_{r_m}^{r_o} 2\lambda_z \frac{\partial W^{(out)}}{\partial \lambda_z} - \lambda_\theta \frac{\partial W^{(out)}}{\partial \lambda_\theta} - 3\gamma \frac{\partial W^{(out)}}{\partial \gamma} r dr = 0 \quad (S22)$$

$$M = 2\pi \int_{r_i}^{r_m} \frac{\partial W^{(in)}}{\partial \gamma} r^2 dr + 2\pi \int_{r_m}^{r_o} \frac{\partial W^{(out)}}{\partial \gamma} r^2 dr = 0 \quad (S23)$$

Taylor Expansion Since Equations (S21)-(S23) are quite complex and it is computationally intensive to solve them numerically, for thin-walled actuators we simplify the calculations by Taylor expanding the equations.

We define $\varepsilon_1 = \frac{R_m - R_i}{R_i}$ and $\varepsilon_2 = \frac{R_o - R_m}{R_m}$, and Taylor expand Equations (S21)-(S23). Our goal was to retain the minimum number of terms required to give an accurate solution. We found that retaining first order terms in ε_2 was sufficient, but for ε_1 , we had to retain terms to third order, since $\varepsilon_1 \gg \varepsilon_2$. This gave us the following system of equations:

$$\begin{aligned} P = & \frac{R_i}{r_i \lambda_z} \frac{\partial W_1}{\partial \lambda_\theta} \varepsilon_1 + \frac{R_m}{r_m \lambda_z} \frac{\partial W_2}{\partial \lambda_\theta} \varepsilon_2 + \frac{1}{2r_i^3 \lambda_z^2} \left[-R_i^3 \frac{\partial W_1}{\partial \lambda_\theta} + r_i(R_i^2 - r_i^2 \lambda_z) \frac{\partial^2 W_1}{\partial \lambda_\theta^2} \right] \varepsilon_1^2 \\ & + \frac{1}{6r_i^5 R_i \lambda_z^3} \left[(3R_i^6 - r_i^2 R_i^4 \lambda_z) \frac{\partial W_1}{\partial \lambda_\theta} - r_i(R_i^2 - r_i^2 \lambda_z) \left((3R_i^3 + 2r_i^2 R_i \lambda_z) \frac{\partial^2 W_1}{\partial \lambda_\theta^2} + r_i(-R_i^2 + r_i^2 \lambda_z) \frac{\partial^3 W_1}{\partial \lambda_\theta^3} \right) \right] \varepsilon_1^3 \\ & + \mathcal{O}(\varepsilon_1^4) + \mathcal{O}(\varepsilon_2^2) \quad (S24) \end{aligned}$$

$$\begin{aligned} N_{ral} = & \frac{R_i \pi}{\lambda_z} \left[2R_i \lambda_z \frac{\partial W_1}{\partial \lambda_z} - r_i \frac{\partial W_1}{\partial \lambda_\theta} \right] \varepsilon_1 + \frac{B \pi}{\lambda_z} \left[2R_m \lambda_z \frac{\partial W_2}{\partial \lambda_z} - r_m \frac{\partial W_2}{\partial \lambda_\theta} \right] \varepsilon_2 \\ & + \frac{\pi}{2r_i \lambda_z^2} \left[2r_i R_i^2 \lambda_z^2 \frac{\partial W_1}{\partial \lambda_z} - R_i^3 \frac{\partial W_1}{\partial \lambda_\theta} + (R_i^2 - r_i^2 \lambda_z) \left(2R_i \lambda_z \frac{\partial^2 W_1}{\partial \lambda_\theta \partial \lambda_z} - r_i \frac{\partial^2 W_1}{\partial \lambda_\theta^2} \right) \right] \varepsilon_1^2 \\ & + \frac{\pi(-R_i^2 + r_i^2 \lambda_z)}{6r_i^3 R_i \lambda_z^3} \left[-R_i^4 \frac{\partial W_1}{\partial \lambda_\theta} + 2R_i^4 \lambda_z \frac{\partial^2 W_1}{\partial \lambda_\theta \partial \lambda_z} + r_i \left((R_i^3 - 2r_i^2 R_i \lambda_z) \frac{\partial^2 W_1}{\partial \lambda_\theta^2} - (R_i^2 - r_i^2 \lambda_z) (2R_i \lambda_z \frac{\partial^3 W_1}{\partial \lambda_\theta^2 \partial \lambda_z} - r_i \frac{\partial^3 W_1}{\partial \lambda_\theta^3}) \right) \right] \varepsilon_1^3 \\ & + \mathcal{O}(\varepsilon_1^4) + \mathcal{O}(\varepsilon_2^2) \quad (S25) \end{aligned}$$

$$\begin{aligned} M = & \frac{2r_i R_i^2 \pi}{\lambda_z} \frac{\partial W_1}{\partial \gamma} \varepsilon_1 + \frac{2r_m R_m^2 \pi}{\lambda_z} \frac{\partial W_2}{\partial \gamma} \varepsilon_2 + \frac{R_i \pi}{r_i \lambda_z^2} \left[(R_i^3 + r_i^2 R_i \lambda_z) \frac{\partial W_1}{\partial \gamma} + r_i(R_i^2 - r_i^2 \lambda_z) \frac{\partial^2 W_1}{\partial \lambda_\theta \partial \gamma} \right] \varepsilon_1^2 + \\ & \frac{\pi}{3r_i^3 \lambda_z^3} \left[-(R_i^6 - 3r_i^2 R_i^4 \lambda_z) \frac{\partial W_1}{\partial \gamma} + r_i(R_i^2 - r_i^2 \lambda_z) \left(R_i^3 \frac{\partial^2 W_1}{\partial \lambda_\theta \partial \gamma} + r_i(R_i^2 - r_i^2 \lambda_z) \frac{\partial^3 W_1}{\partial \lambda_\theta^2 \partial \gamma} \right) \right] \varepsilon_1^3 \\ & + \mathcal{O}(\varepsilon_1^4) + \mathcal{O}(\varepsilon_2^2) \quad (S26) \end{aligned}$$

As shown in Figure S6, this expansion is valid for $\epsilon_1 \leq 0.47$ (Figure S6A,B). However, as ϵ_1 increases, the Taylor expansion becomes less accurate. This is shown in Figure S6C, where we have $\epsilon_1 = 0.63$, and observe that the Taylor expansion deviates significantly from the full solution.

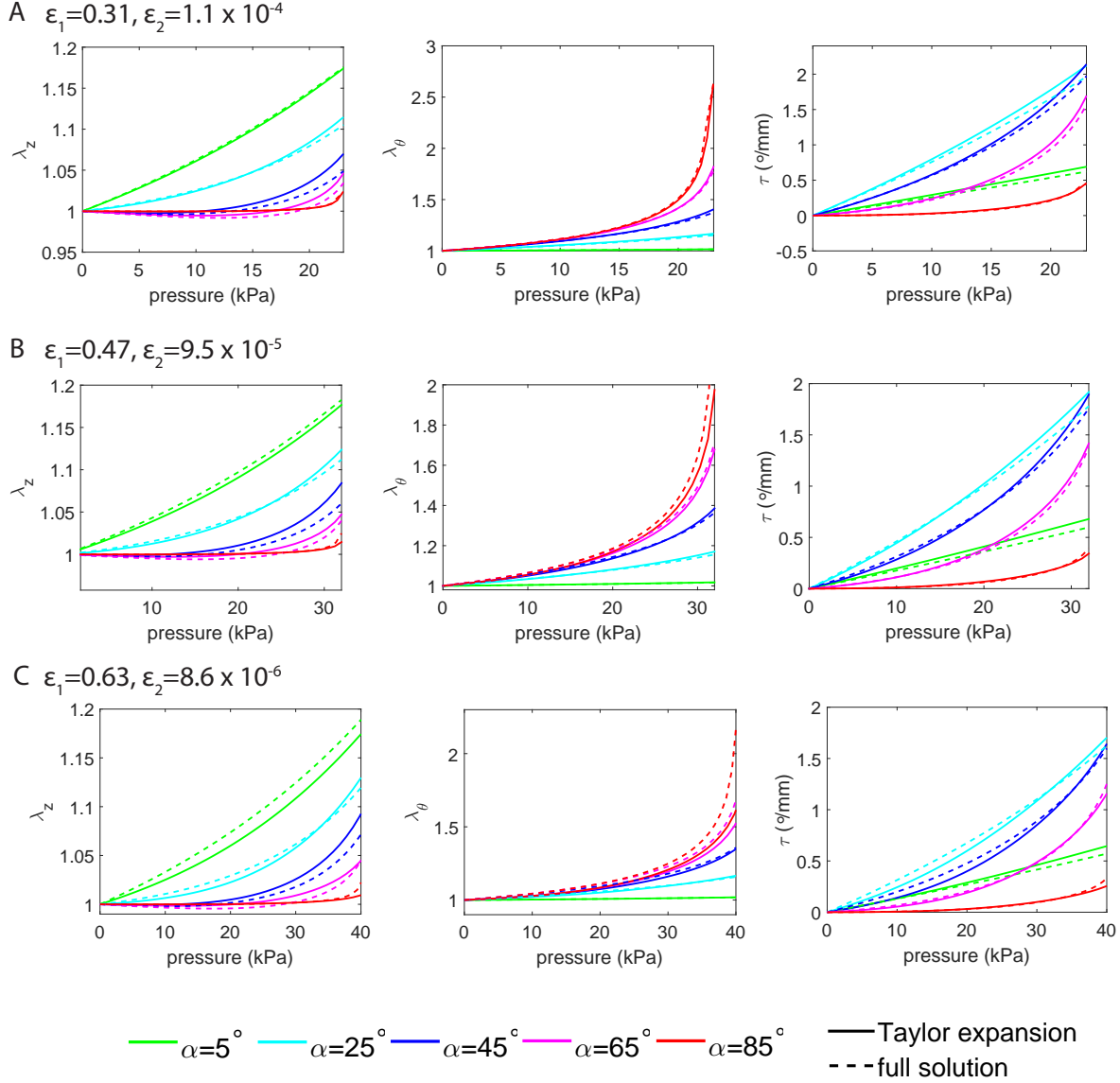


Figure S6: Comparison of solution using full system of equations (Equations (19)-(21)) with solution using Taylor expanded equations (Equations (22)-(24)). (A) Results for an actuator with ratios $\epsilon_1 = 0.31$ and $\epsilon_2 = 1.1 \times 10^{-4}$. (B) Results for an actuator with ratios $\epsilon_1 = 0.47$ and $\epsilon_2 = 9.5 \times 10^{-5}$. In each of these cases, we see that the Taylor expansion provides a close approximation to the full solution. However, for a thicker-walled actuator, the Taylor expansion becomes less accurate. This is shown in (C), where we have ratios $\epsilon_1 = 0.63$ and $\epsilon_2 = 8.6 \times 10^{-6}$, and observe that the Taylor expansion deviates significantly from the full solution.

S3.2.1 Verification of the Model

To verify the analytical model for actuators which extend, expand, and twist, we fabricated some actuators from Dragon Skin 10 and from Smooth-Sil 950. In Figure S7, we compare the analytical prediction to the experimental results for two actuators ($\alpha = 3^\circ$ and $\alpha = 70^\circ$) for each material. Each actuator had inner

radius $R_i = 6.35\text{mm}$, wall thickness $R_o - R_i = 2\text{mm}$, and length $L = 160\text{mm}$. The number of fibers was $n = \text{round}(13 \sin \alpha)$, and the fibers had radius $r = 0.0889\text{mm}$ and Young's modulus $E = 31067\text{MPa}$. We found that the response of the actuators was best captured choosing the fitting parameter $R_o - R_m = 8.89 \times 10^{-4}\text{mm}$, so that $\epsilon_1 = 0.31$ and $\epsilon_2 = 1.1 \times 10^{-4}$. For this choice of R_m the volume fractions were $c_1 = \frac{\pi(R_o^2 - R_m^2)L}{\pi(R_o^2 - R_m^2)L + n \times \pi r^2 \times \frac{L}{\sin \alpha}}$ and $c_2 = \frac{n \times \pi r^2 \times \frac{L}{\sin \alpha}}{\pi(R_o^2 - R_m^2)L + n \times \pi r^2 \times \frac{L}{\sin \alpha}}$. In each case shown in Figure S7, we see good agreement between the analytical prediction and the experimental results. Some deviations in Figure S7A are most likely due to inaccuracies in the fabrication procedure. We also see some deviations at higher pressures in Figure S7B due to the highly nonlinear response of the actuators.

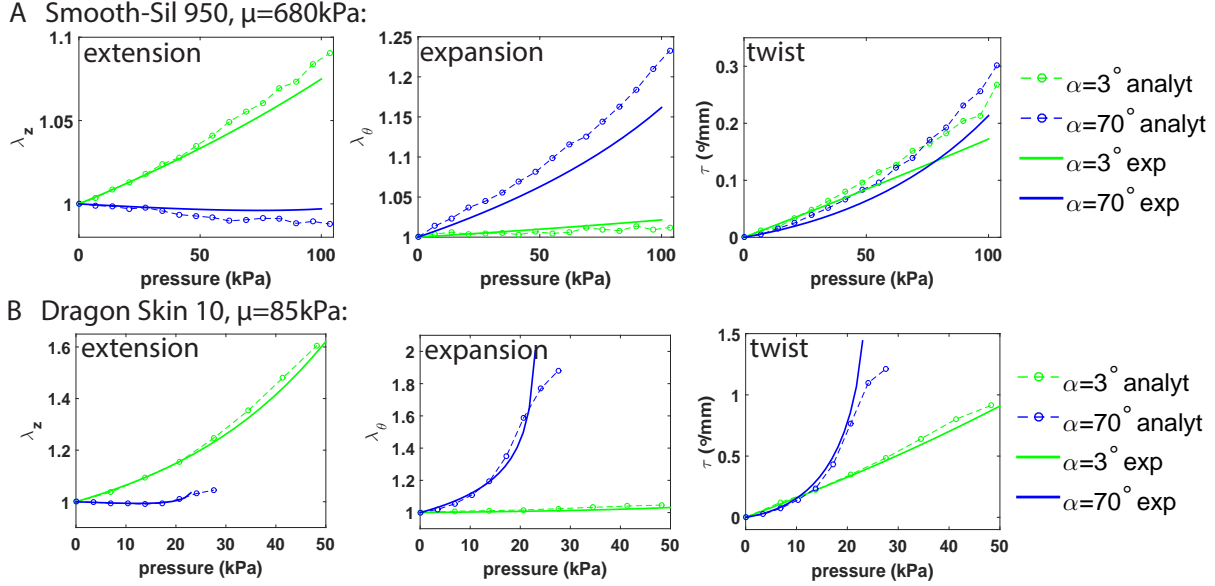
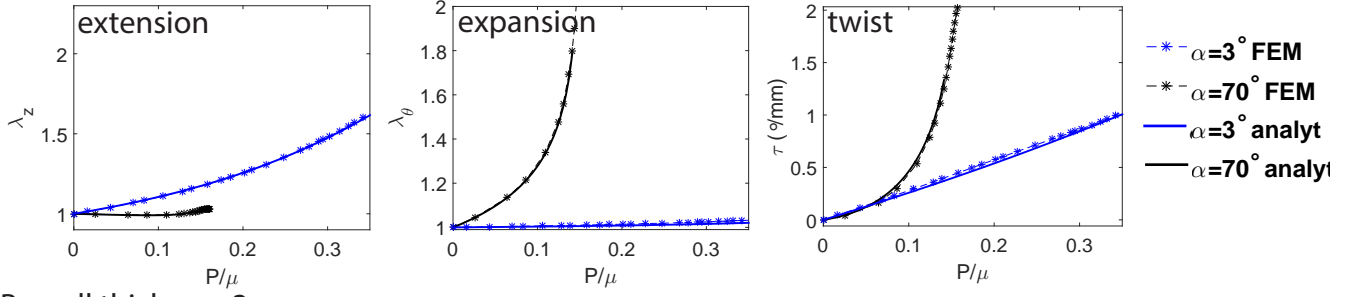


Figure S7: Comparison of experimental results and analytical predictions for (A) Smooth-Sil 950 and (B) Dragon Skin 10. For each material, two actuators are shown: one with fiber angle $\alpha = 3^\circ$ and one with fiber angle $\alpha = 70^\circ$. Axial stretch λ_z (left), radial stretch λ_θ (center), and twist per unit length τ (right) are shown in each case.

We used Finite Element analysis to verify that the model is valid for actuators with different wall thicknesses (see Figure S8). Each actuator had inner radius $R_i = 6.35\text{mm}$, and length $L = 160\text{mm}$. Wall thicknesses were either $R_o - R_i = 1\text{mm}$ or $R_o - R_i = 3\text{mm}$ and materials were either Dragon Skin 10 or Smooth-Sil 950, as shown in Figure S8. Also in this case we chose $R_o - R_m = 8.89 \times 10^{-4}\text{mm}$, so that $\epsilon_1 = 0.16$ and $\epsilon_2 = 1.2 \times 10^{-4}$ for the thinner actuator and $\epsilon_1 = 0.47$ and $\epsilon_2 = 9.5 \times 10^{-5}$ for the thicker one. In each case, we see excellent agreement between the analytical predictions and the Finite Element results.

A wall thickness 1mm:



B wall thickness 3mm:

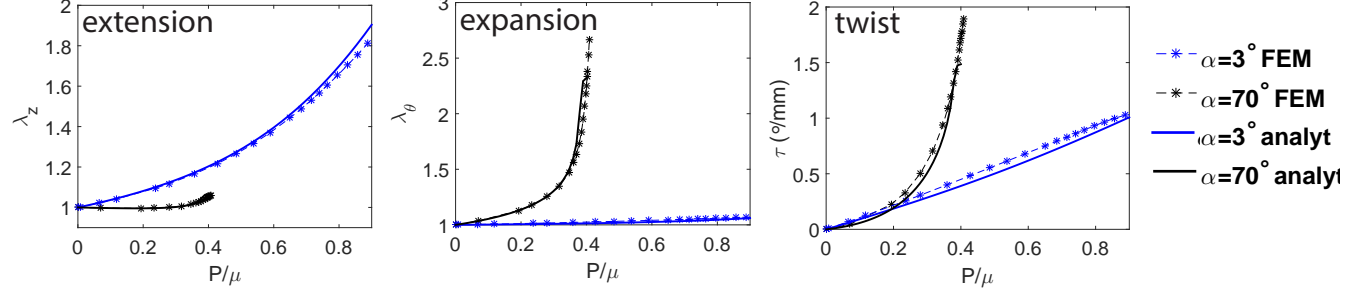


Figure S8: Verification of extend/expand/twist model for Dragonskin 10, for wall thicknesses of 1mm and 3mm. For each wall thickness, two actuators are shown: one with fiber angle $\alpha = 3^\circ$ and one with fiber angle $\alpha = 70^\circ$. Axial stretch λ_z (left), radial stretch λ_θ (center), and twist per unit length τ (right) are shown in each case.

S3.3 Modeling bending

Since the exact solution for the finite bending of an elastic body is only possible under the assumption that the cross-sections of the cylinder remain planar upon pressurization - a condition that is severely violated by our actuator - we assume (i) that the radial expansion can be neglected (i.e. $r/R = 1$) and (ii) vanishing stress in the radial direction (i.e. $\sigma_{rr} = 0$). Furthermore, since the actuators have a symmetric arrangement of fibers, no twisting takes place, so the deformation gradient reduces to

$$\mathbf{F} = \begin{pmatrix} \lambda_z(\phi)^{-1} & 0 & 0 \\ 0 & 1 & 0 \\ 0 & 0 & \lambda_z(\phi) \end{pmatrix}. \quad (\text{S27})$$

Since the actuator bends due to the moment created by the internal pressure acting on the actuator caps, M_{cap} , the relationship between input pressure and bend angle can be found by equating M_{cap} to the opposing moment due to the stress in the material, M_{mat} .

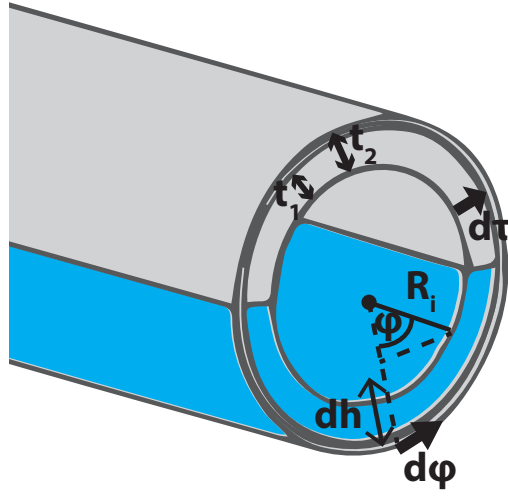


Figure S9: Cross section of the actuator, with inner radius R_i . The thickness of the inner layer is t_1 , and total wall thickness is t_2 . The differential angle element is $d\phi$, differential wall thickness element is $d\tau$, and differential height is dh .

Calculating M_{cap} To calculate the moment (M_{cap}) due to air pressure acting on the internal cap of the actuator, we start by noting that the force due to the air pressure acting on an infinitesimal area of the actuator cap $dA = 2R_i \sin \phi dh$ is

$$df = P dA = P 2R_i \sin \phi dh, \quad (\text{S28})$$

where P is the internal pressure in the actuator, and $d\phi$ and dh are the differential angle and height respectively, as shown in Figure S9. By re-writing h in terms of ϕ as

$$h = R_i - R_i \cos \phi \Rightarrow dh = R_i \sin \phi d\phi, \quad (\text{S29})$$

we can eliminate h from Equation (S28)

$$df = P 2R_i^2 \sin^2 \phi d\phi. \quad (\text{S30})$$

The moment acting on the cap is then

$$\begin{aligned} M_{cap} &= \int_0^{2R_i} df \times \text{distance from neutral axis} \\ &= 2PR_i^2 \int_0^\pi \sin^2 \phi \text{abs} [R_i \cos \bar{\phi} - R_i \cos \phi] d\phi, \end{aligned} \quad (\text{S31})$$

where $\bar{\phi}$ indicates the position of the neutral axis.

Calculating M_{mat} The moment due to the stress in the material, M_{mat} , is

$$\begin{aligned}
M_{mat} = & 2 \int_0^{t_1} \int_{\frac{\pi}{2}}^{\pi} \lambda_z(\phi)^{-1} \sigma_{zz}^{(in,1)}(R_i + \tau) (R_i \cos \bar{\phi} - (R_i + \tau) \cos \phi) d\phi d\tau \\
& + 2 \int_{t_1}^{t_2} \int_{\frac{\pi}{2}}^{\pi} \lambda_z(\phi)^{-1} \sigma_{zz}^{(out,1)}(R_i + \tau) (R_i \cos \bar{\phi} - (R_i + \tau) \cos \phi) d\phi d\tau \\
& + 2 \int_0^{t_1} \int_0^{\frac{\pi}{2}} \lambda_z(\phi)^{-1} \sigma_{zz}^{(in,2)}(R_i + \tau) (R_i \cos \bar{\phi} - (R_i + \tau) \cos \phi) d\phi d\tau \\
& + 2 \int_{t_1}^{t_2} \int_0^{\frac{\pi}{2}} \lambda_z(\phi)^{-1} \sigma_{zz}^{(out,2)}(R_i + \tau) (R_i \cos \bar{\phi} - (R_i + \tau) \cos \phi) d\phi d\tau
\end{aligned} \tag{S32}$$

where $\sigma_{zz}^{(in,i)}$ is the axial stress in the inner isotropic layer with shear modulus μ_i :

$$\sigma_{zz}^{(in,i)} = \lambda_z^2 \mu_i - \frac{\mu_i}{\lambda_z^2} \tag{S33}$$

and $\sigma_{zz}^{(out,i)}$ is the axial stress in the outer anisotropic layer with shear modulus μ_i :

$$\begin{aligned}
\sigma_{zz}^{(out,i)} = & \lambda_z^2 \mu_i - \frac{\mu_i}{\lambda_z^2} + \frac{2}{\sqrt{I_4}} \left[(-1 + \sqrt{I_4}) \lambda_z^2 \rho_1 \sin^2[\alpha] \right] \\
& + \frac{2}{\sqrt{I_6}} \left[(-1 + \sqrt{I_6}) \lambda_z^2 \rho_2 \sin^2[\alpha] \right]
\end{aligned} \tag{S34}$$

The parameter t_1 is the thickness of the inner isotropic layer ($R_m - R_i$), t_2 is the total wall thickness of the actuator ($R_o - R_i$), and $d\tau$ is the differential thickness of the actuator (Figure S9).

S3.3.1 Obtaining the relationship between input pressure and bend angle

Now solving $M_{mat} = M_{cap}$ yields the relationship between input pressure and output bend angle:

$$\begin{aligned}
P = & \frac{\int_0^{t_1} \int_{\frac{\pi}{2}}^{\pi} \lambda_z^{-1} \sigma_{zz}^{(in,1)}(R_i + \tau) (R_i \cos \bar{\phi} - (R_i + \tau) \cos \phi) d\phi d\tau + \int_{t_1}^{t_2} \int_{\frac{\pi}{2}}^{\pi} \lambda_z^{-1} \sigma_{zz}^{(out,1)}(R_i + \tau) (R_i \cos \bar{\phi} - (R_i + \tau) \cos \phi) d\phi d\tau}{2R_i^2 \int_0^{\pi} \sin^2 \phi \text{abs} (R_i \cos \bar{\phi} - R_i \cos \phi) d\phi} \\
& + \frac{\int_0^{t_1} \int_0^{\frac{\pi}{2}} \lambda_z^{-1} \sigma_{zz}^{(in,2)}(R_i + \tau) (R_i \cos \bar{\phi} - (R_i + \tau) \cos \phi) d\phi d\tau + \int_{t_1}^{t_2} \int_0^{\frac{\pi}{2}} \lambda_z^{-1} \sigma_{zz}^{(out,2)}(R_i + \tau) (R_i \cos \bar{\phi} - (R_i + \tau) \cos \phi) d\phi d\tau}{2R_i^2 \int_0^{\pi} \sin^2 \phi \text{abs} (R_i \cos \bar{\phi} - R_i \cos \phi) d\phi}
\end{aligned} \tag{S35}$$

S3.3.2 Locating the neutral bending axis

In the bending model, the parameter $\bar{\phi}$ is the circumferential angle where the neutral bending axis is located. This parameter was determined using an FE simulation for an actuator with fiber angle $\pm 5^\circ$,

$R_i = 6.35mm$, $R_o = 8.35mm$, and $L = 160mm$. We found the neutral bending axis occurs at $\bar{\phi} = 35^\circ$, as shown in Figure S10A, where we plot the axial stretch along the line corresponding to $\bar{\phi} = 35^\circ$, and compare it to the maximum axial stretch (which occurs at $\phi = 180^\circ$). To demonstrate that $\bar{\phi}$ does not depend on the fiber angle, we also extracted the axial stretch at 35° for actuators with fiber angles $\pm 15^\circ$ and $\pm 25^\circ$ (Figure S10B).

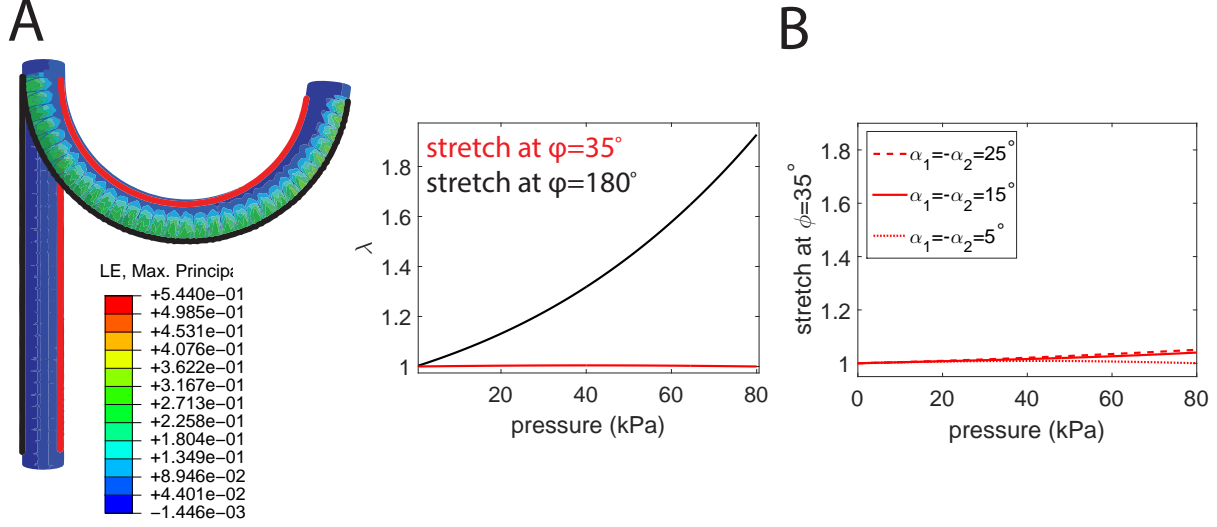


Figure S10: (A) FEA results for a bending actuator with fiber angle $\alpha = \pm 5^\circ$, at $P = 0kPa$ and $P = 40kPa$. The material line at $\phi = 180^\circ$ is highlighted in black, and the line at $\phi = 35^\circ$ is highlighted in red. The graph shows the corresponding axial stretches. We see that at $\phi = 35^\circ$, the actuator does not change in length. (B) Comparison of axial stretch at $\phi = 35^\circ$ for bending actuators with fiber angles $\alpha = \pm 5^\circ$, $\alpha = \pm 15^\circ$ and $\alpha = \pm 25^\circ$. In each case, the stretch is almost unity, showing that we can use the line at $\bar{\phi} = 35^\circ$ as the neutral axis.

S3.3.3 Verification of Bending Model

To verify the analytical bending model, we performed FE simulations and compared the results to the analytical predictions, as shown in Figure S11. In each case (A-D), we used one FE simulation ($\alpha = \pm 5^\circ$) to find the location of the neutral axis $\bar{\phi}$. For case A, the thickness of the outer layer, $R_o - R_m$, was a fitting parameter found using the extend/expand/twist model. For the other cases, this value was reduced in proportion to the wall thickness to outer radius ratio (e.g. in case B, the ratio was reduced to 0.66 of its initial value, so we also reduced the thickness of the outer layer by this amount).

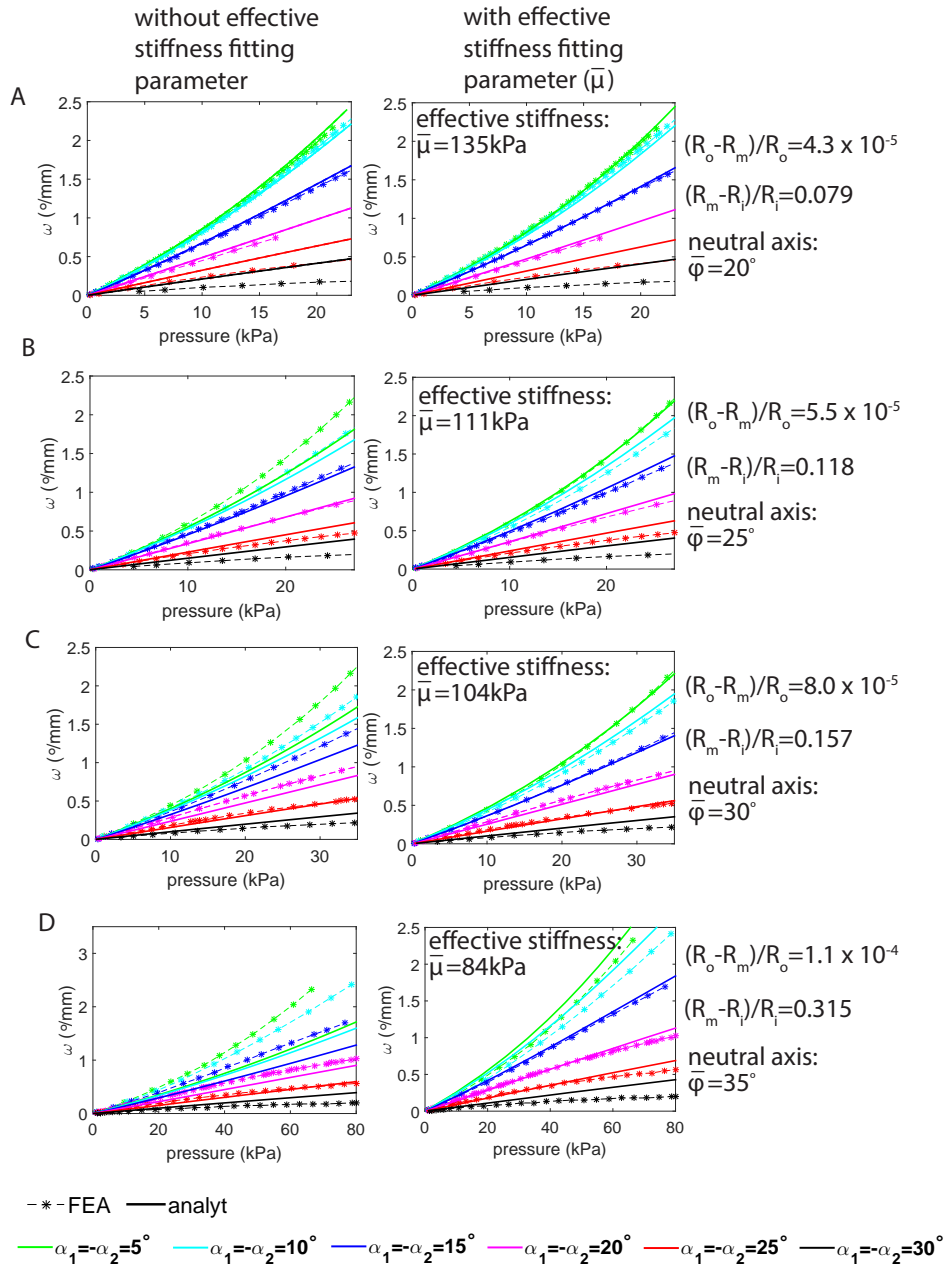


Figure S11: Comparing analytical results to FEA results for various different wall thickness to radius ratios. The column on the left shows results obtained from the model using the experimentally measured moduli, while the column on the right shows results obtained using an effective modulus $\bar{\mu}$ (fitted using an FE simulation). As the wall thickness to radius ratio decreases (going from A to D), the analytical model becomes much more accurate. In case D, we see that the ratio is small enough that there is no need to use an effective stiffness, as it gives the same results as using the experimentally measured moduli (i.e. for case D, the graphs in the left and right columns are the same).

When deriving the bending model, we assumed that the actuator walls were thin. As a result, for thicker walled actuators, the model yields lower than expected bend angles at any given pressure, because the actuators are too stiff. This can be seen in the left column of Figure S11, which compares analytical and FE results for actuators with various different ratios of wall thickness to outer radius. We see that as the thickness to radius ratio decreases, the model gives more accurate results.

In order to use the model for actuators with higher thickness to radius ratios, we use an effective shear

modulus in the model, rather than using the experimentally measured moduli. This is illustrated in the right column of Figure S11. One FE simulation ($\alpha = \pm 5^\circ$) is used to find the effective shear modulus. Using this fitting parameter (from just one simulation), we can quite accurately predict the deformation for other fiber angles. As the ratio decreases, we see that there is no need to use this fitting parameter, since in case D, it gives almost identical results to when the experimentally measured shear moduli are used.

To experimentally verify the bending model, we fabricated and tested bending actuators with fiber angles ranging from $\pm 5^\circ$ to $\pm 30^\circ$. The actuators had inner radius $R_i = 6.35mm$, wall thickness $R_o - R_i = 2mm$, and length $L = 160mm$. Using $R_m = 8.89 \times 10^{-4}mm$ and effective shear modulus $\bar{\mu} = 78kPa$, we found good agreement between the analytical model and the experimental results (Figure S12).

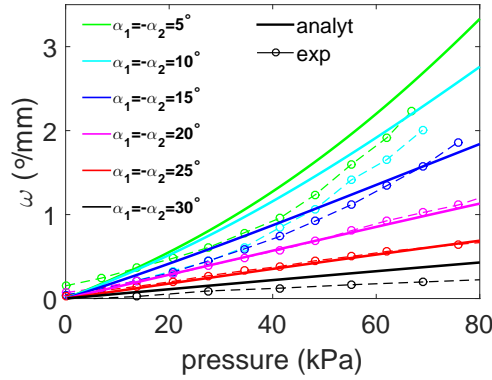


Figure S12: Comparison of experimental results and analytical predictions of bend angle per unit length for actuators with fiber angles ranging from $\pm 5^\circ$ to $\pm 30^\circ$

S4 Replicating Finger Motion

In this section, we describe the procedure for gathering and processing the data describing the kinematics of the fingers. We then describe the steps in the optimization algorithm which is used to determine the optimal design parameters for an actuator which, upon pressurization, will replicate the motion of the fingers. We use the optimization algorithm to design actuators which replicate the motion of the index finger and the thumb, and verify the results using finite element analysis. Finally, we outline the experimental procedure for determining the motion of an actuator in 3d space. Note that the Matlab scripts corresponding to this section can be found on softroboticstoolkit.com.

S4.1 Processing the input data

We use electromagnetic (EM) trackers to record the coordinates of the index finger and thumb as they bend. The location of the EM trackers on the hand is illustrated in Figure S13A. The lengths of each of

the links and the angles between the links are plotted as a function of time in Figure S14 (index finger) and Figure S15 (thumb).

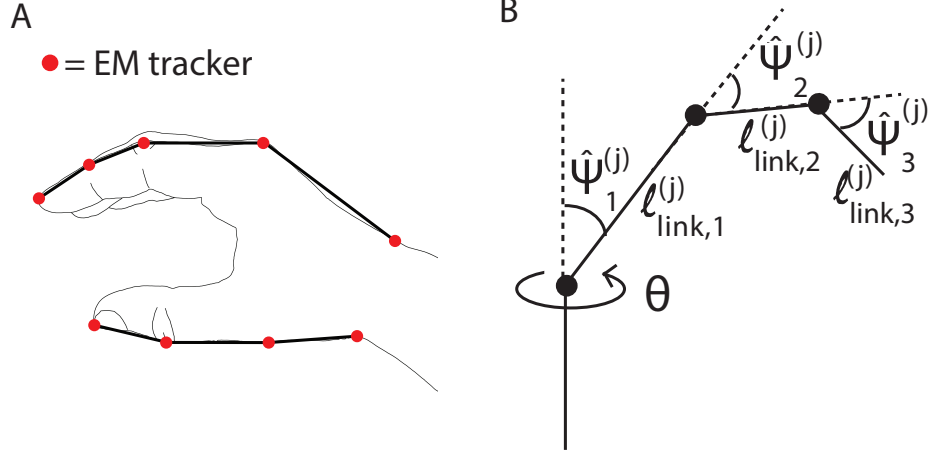


Figure S13: (A) Location of the EM trackers on the index finger and thumb (B) The link lengths $l_{link,i}$ are the lengths between the joints of the finger, while the bend angles $\hat{\psi}_i$ are the angles between adjacent links, as illustrated above.

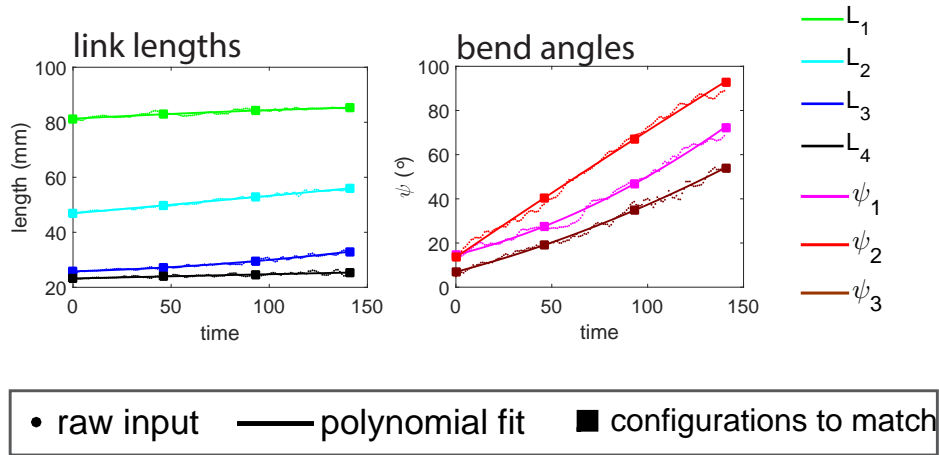


Figure S14: Index finger EM tracker data: The dots represent the raw input. This is smoothed using a Savitzky-Golay filter in Matlab, and the smoothed data are plotted as solid lines. Solid squares denote the four configurations which are selected to be replicated.

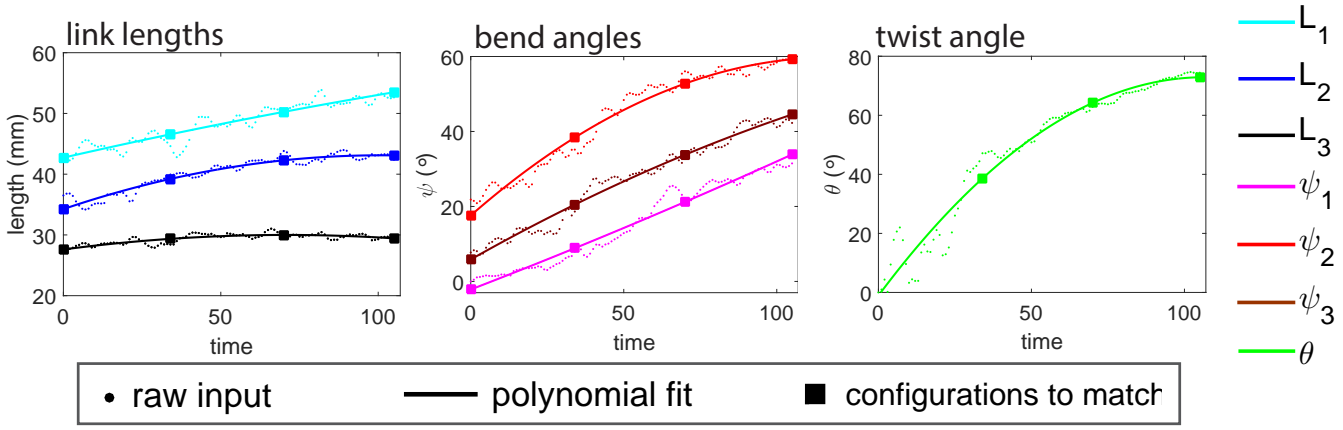


Figure S15: Thumb EM tracker data: The dots represent the raw input. This is smoothed using a Savitzky-Golay filter in Matlab, and the smoothed data are plotted as solid lines. Solid squares denote the four configurations which are selected to be replicated.

S4.2 Optimization

We want the optimization to output (1) the fiber angle α_i for each segment (2) the initial length $l_{bend,i}^{(0)}$ of each of the bending segments and (3) the pressures $P^{(j)}$ at which the input configurations will occur i.e. we want to find the values of the variables α_i , $l_{bend,i}^{(0)}$ and $P^{(j)}$ which will achieve the desired link lengths and bend angles. For the initial values of the variables, we choose pressures equally spaced between the minimum pressure ($0kPa$) and maximum pressure ($80kPa$), and since we want the bend and twist segment lengths to be as short as possible, we set α_i and $l_{bend,i}^{(0)}$ to their minimum allowed values $\alpha_i = \alpha_{min} = 5^\circ$, $l_{bend,i}^{(0)} = L_{min} = 10mm$.

The maximum allowed bend segment length was chosen by doing some preliminary calculations: The maximum bend angle required for the index finger was 93° , and the bend angle per unit length for an actuator with fiber angle 5° at the maximum allowed pressure $P_{max} = 80kPa$ is $3.3^\circ/mm$. Dividing the maximum required bend angle by the maximum possible bend per unit length gave a segment length of $28mm$. This was rounded up to give a maximum allowed segment length of $30mm$.

The main steps in the optimization are as follows:

Step 1

- Given the fiber angle α for each segment and bending and twisting segment lengths, calculate the initial lengths of the extending segments, as shown in Figure 4 (for example, $\hat{l}_{ext,2}^{(0)} = l_{link,2}^{(0)} - \frac{l_{bend,2}^{(0)}}{2} - \frac{l_{bend,4}^{(0)}}{2}$).
- Calculate the extension of the bending segments in each configuration (for example, $l_{bend,2}^{(j)} = l_{bend,2}^{(0)} + R_i \psi_2^{(j)} (\cos \bar{\phi} + 1)$, where R_i is the inner radius of the actuator).

- Use the bend segment lengths in each configuration and the overall link lengths in each configuration to calculate the required length of each of the extending segments in each configuration (for example, $\hat{l}_{ext,2}^{(j)} = l_{link,2}^{(j)} - \frac{l_{bend,2}^{(j)}}{2} - \frac{l_{bend,4}^{(j)}}{2}$).

Step 2

- For each extending (or twisting) segment, given the fiber angle α_i , use the analytical model to solve for the segment length \hat{l} (or twist $\hat{\theta}$) at each pressure $P^{(j)}$.
- The bending model is an inverse model (given a bend angle, it outputs the pressure at which that bend angle is achieved). So, for each bending segment, given the fiber angle α_i , use the analytical model to find the pressures $\hat{P}^{(j)}$ at which the required bend angles ψ are achieved.

Step 3

The function to be minimized is

$$\begin{aligned}
f = & c_1 \sum_{j=1}^N \sum_{i=1}^{n_{tw}} \left| \theta_i^{(j)} - \hat{\theta}_i^{(j)} \right|^2 + \sum_{j=1}^N \sum_{i=1}^{n_{ext}} \left| l_{ext,i}^{(j)} - \hat{l}_{ext,i}^{(j)} \right|^2 \\
& + c_2 \sum_{j=1}^N \sum_{i=1}^{n_{bend}} \left| P_i^{(j)} - \hat{P}^{(j)} \right|^2,
\end{aligned} \tag{S36}$$

where n_{tw} , n_{ext} and n_{bend} are the total number of twisting, extending, and bending segments, respectively, and N is the number of goal configurations. If f is not sufficiently small, x is updated and the steps are repeated. When the minimum value of f is found, the fiber angles, segment lengths, and pressures are output.

S4.3 Glove

In the main text, we used the optimization algorithm to design an actuator where the *top* of the actuator mimics the input motion. Here, we use the algorithm to design an actuator where the *bottom* of the actuator mimics the input motion. This could be used to design an actuator for use in an assistive glove, for example [5]. We follow the same procedure as before. The twist and bend angles to be matched are the same as in the main text, but now the link lengths should be matched by the bottom edge of the actuator.

S4.3.1 Index finger

For the index finger, the optimization determined that the actuator should have extending segments 1, 3, and 6, with lengths 70mm, 21mm, and 16mm respectively, and fiber angles $\pm 33^\circ$, $\pm 15^\circ$, and $\pm 27^\circ$

respectively, and bending segments 2, 4, and 5 with lengths 23mm, 28mm, and 15mm respectively, and fiber angles $\pm 8.1^\circ$, $\pm 5^\circ$, and $\pm 5^\circ$ respectively. We used FEA to investigate the response of an actuator with this design, and we see in Figure S16 that the FE results are in good agreement with the analytical prediction.

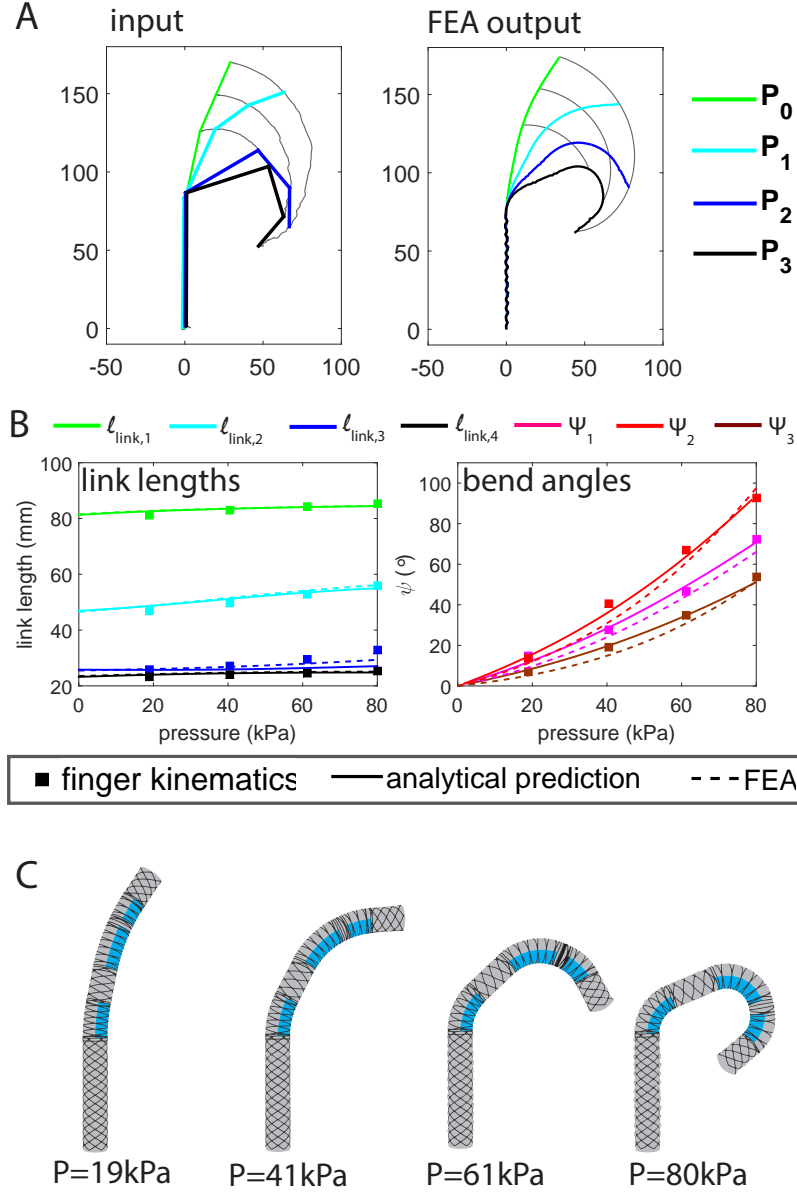


Figure S16: (A) Desired input configurations (left) and achieved FEA output configurations (right) (B) Comparing the input configurations, analytical prediction, and FEA output for each link length and bend angle (C) FEA results for each of the four configurations

S4.3.2 Thumb

As a second example, we consider the motion of the thumb. This time the optimization determines that the actuator should have a twisting segment 1 with length 24mm and fiber angle 5° , extending segments 3, 5, and 7, with lengths 21mm, 9mm, and 17mm respectively and fiber angles $\pm 8^\circ$, $\pm 5^\circ$, and $\pm 25^\circ$ respectively, and bending segments 2, 4, and 6, with lengths 14mm, 30mm, and 21mm respectively, each with fiber

angle $\pm 5^\circ$. Again, we use FEA to analyze the result, and Figure S17 shows that the FE results and the analytical prediction match closely.

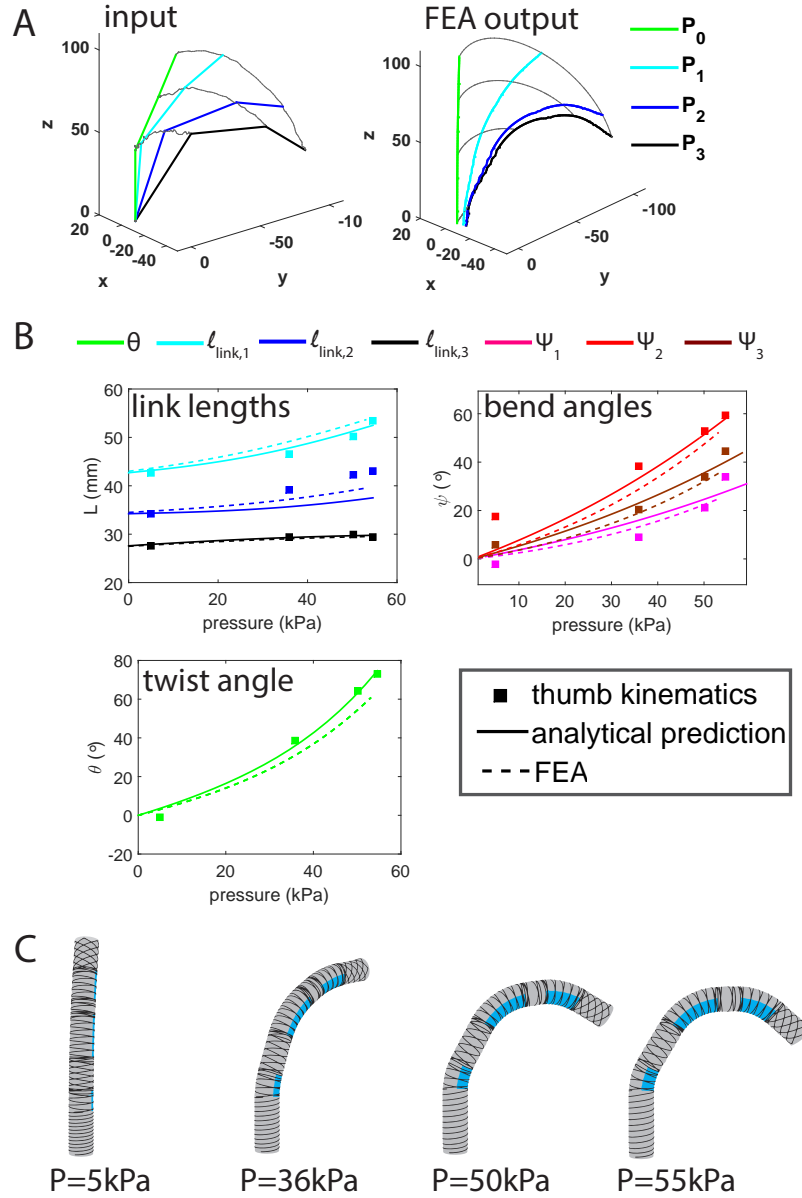


Figure S17: (A) Desired input configurations (left) and achieved FEA output configurations (right) (B) Comparing the input configurations, analytical prediction, and FEA output for each link length and bend angle, and for the twist angle (C) FEA results for each of the four configurations

S4.4 Thumb actuator: reconstructing 3d motion

Here we describe our procedure for recording the motion of the thumb actuator. Since the thumb actuator moves out of plane, tracking its motion is slightly more complex than in the case of the finger actuator. In previous cases, we took a photograph of the actuator at each pressure increment. Now, at each pressure increment, we take photographs of the actuator from two perspectives, using cameras positioned at right angles to one another (Figure S18A,C). We post-process the photographs by using Matlab to track the left

and right edges of the actuator in each picture. We then find the center line of the actuator by calculating the average of the left and right sides (Figure S18B,D). Finally, we interpolate the center line, so that the front view and the side view are sampled at identical z values. We can then combine the $x - z$ data and the $y - z$ data to find the $x - y - z$ data (Figure S18E).

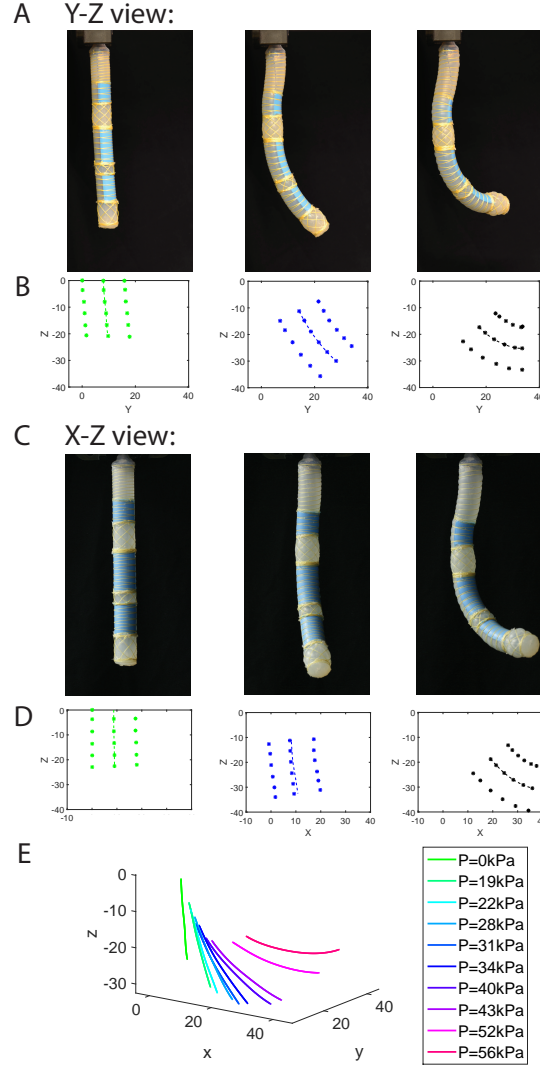


Figure S18: Reconstructing the motion of segment 6 of the thumb actuator: (A) Front view of the actuator at 3 different actuation pressures (B) Points on either side of the actuator are tracked in Matlab, and used to find the center line (C) Side view of the actuator at 3 different actuation pressures (D) Points on either side of the actuator are tracked in Matlab, and used to find the center line (E) X - Y and Y - Z values are combined to find the configurations in X - Y - Z

S5 Video legends

Video S1: A comparison of index finger motion with an actuator designed to replicate this motion.

Video S2: A comparison of thumb motion with an actuator designed to replicate this motion.

References

- [1] J. E. Adkins and R. S. Rivlin, *Large elastic deformations of isotropic materials X. Reinforcement by inextensible cords*, Phil. T Royal Soc A, 248 (1955), pp. 201–223.
- [2] F. Kassianidis, *Boundary-value problems for transversely isotropic hyperelastic solids*, Thesis, University of Glasgow, (2007).
- [3] A. Goriely and M. Tabor, *Rotation, inversion, and perversion in anisotropic elastic cylindrical tubes and membranes*, Proc Royal Soc A, 469 (2013), pp. 20130011.
- [4] R. W. Ogden. *Non-Linear Elastic Deformations*, Dover, New York, 1984.
- [5] P. Polygerinos, Z. Wang, K. C. Galloway, R. J. Wood and C. J. Walsh. *Soft Robotic Glove for Combined Assistance and at-Home Rehabilitation*, Robot Auton Syst 73 (2015), pp. 139.